ARL-TR-9422 • MAR 2022

Development of Diamond-Based Materials Systems for High-Power RF Electronics: Second-Year Report

by Pulickel M Ajayan, Robert Vajtai, Xiang Zhang, Anand B Puthirath, Abhijit Biswas, Eliezer Oliveira, Chenxi Li, Harikishan Kannan, Tia Gray, Tony Ivanov, A Glen Birdwell, Dmitry Ruzmetov, Mahesh Neupane, Pankaj Shah, Sergey Rudin, James Weil, Leonard De La Cruz, Derwin Washington, Stephen B Kelley, and Bradford B Pate

Approved for public release: distribution unlimited.

NOTICES

Disclaimers

The findings in this report are not to be construed as an official Department of the Army position unless so designated by other authorized documents.

Citation of manufacturer's or trade names does not constitute an official endorsement or approval of the use thereof.

Destroy this report when it is no longer needed. Do not return it to the originator.

ARL-TR-9422 ● MAR 2022

Development of Diamond-Based Materials Systems for High-Power RF Electronics: Second-Year Report

Pulickel Ajayan, Robert Vajtai, Xiang Zhang, Anand B Puthirath, Abhijit Biswas, Eliezer Oliveira, Chenxi Li, Harikishan Kannan, and Tia Gray
Materials Science and NanoEngineering, Rice University

Tony Ivanov, A Glen Birdwell, Dmitry Ruzmetov, Mahesh Neupane, Pankaj Shah, Sergey Rudin, Leonard De La Cruz, and Derwin Washington
DEVCOM Army Research Laboratory

James Weil
Fibertek

Stephen B Kelly
General Technical Services

Bradford B Pate
Nanomaterial Interfaces and Devices, Chemistry Division,
Naval Research Laboratory

Approved for public release: distribution unlimited.

REPORT DOCUMENTATION PAGE			*Form Approved OMB No. 0704-0188*

Public reporting burden for this collection of information is estimated to average 1 hour per response, including the time for reviewing instructions, searching existing data sources, gathering and maintaining the data needed, and completing and reviewing the collection information. Send comments regarding this burden estimate or any other aspect of this collection of information, including suggestions for reducing the burden, to Department of Defense, Washington Headquarters Services, Directorate for Information Operations and Reports (0704-0188), 1215 Jefferson Davis Highway, Suite 1204, Arlington, VA 22202-4302. Respondents should be aware that notwithstanding any other provision of law, no person shall be subject to any penalty for failing to comply with a collection of information if it does not display a currently valid OMB control number.
PLEASE DO NOT RETURN YOUR FORM TO THE ABOVE ADDRESS.

1. REPORT DATE *(DD-MM-YYYY)*	**2. REPORT TYPE**	**3. DATES COVERED (From - To)**
March 2022	Technical Report	November 2020–December 2021

4. TITLE AND SUBTITLE	**5a. CONTRACT NUMBER**
Development of Diamond-Based Materials Systems for High-Power RF Electronics: Second-Year Report	**5b. GRANT NUMBER**
	5c. PROGRAM ELEMENT NUMBER
6. AUTHOR(S)	**5d. PROJECT NUMBER**
Pulickel M Ajayan, Robert Vajtai, Xiang Zhang, Anand B Puthirath, Abhijit Biswas, Eliezer Oliveira, Chenxi Li, Harikishan Kannan, Tia Gray, Tony Ivanov, A Glen Birdwell, Dmitry Ruzmetov, Mahesh Neupane, Pankaj Shah, Sergey Rudin, James Weil, and Leonard De La Cruz, Derwin Washington, Stephen B Kelley, and Bradford B Pate	**5e. TASK NUMBER**
	5f. WORK UNIT NUMBER
7. PERFORMING ORGANIZATION NAME(S) AND ADDRESS(ES)	**8. PERFORMING ORGANIZATION REPORT NUMBER**
Rice University 6100 Main St. Houston, TX 77005	
9. SPONSORING/MONITORING AGENCY NAME(S) AND ADDRESS(ES)	**10. SPONSOR/MONITOR'S ACRONYM(S)**
DEVCOM Army Research Laboratory ATTN: FCDD-RLS-ER 2800 Powder Mill Rd Adelphi, MD 20783	DEVCOM ARL
	11. SPONSOR/MONITOR'S REPORT NUMBER(S)
	ARL-TR-9422

12. DISTRIBUTION/AVAILABILITY STATEMENT
Approved for public release: distribution unlimited.

13. SUPPLEMENTARY NOTES
ORCID IDs: A Glen Birdwell, 0000-0001-5235; Tony Ivanov, 0000-0002-1472-788X; Mahesh Neupane, 0000-0002-4806-6581; Dmitry Ruzmetov 0000-0002-0688-1908; James Weil 0000-0001-8125-4587

14. ABSTRACT
The report details second-year research effort that is part of the Cooperative Agreement between Rice University and the US Army Combat Capabilities Development Command Army Research Laboratory. The project aims to develop diamond and diamond-based heterostructures for the next generation of ultra-wide-bandgap electronic devices, with performances far exceeding existing diamond devices as well as other wide-bandgap materials–based devices. The Rice team focuses on the growth of high-quality single-crystal diamond substrates, heterostructures of diamond, and boron nitride; and the DEVCOM Army Research Laboratory is building high-performance electronic devices based on diamond, specifically using transfer doping of hydrogenated diamond surfaces. Rice has established a world-class facility to grow single-crystal diamond and heterostructures. First- and second-year work has included growth and transfer of boron nitride on commercially available diamond substrates, doping using ion implantation, deposition of the boron nitride structure on diamond, development of unique metrology tools to characterize diamond surfaces, heterostructures, surface modification using hydrogenation and oxygenation, and theoretical models to understand the growth, adhesion energy, and surface characteristics of diamond and diamond–boron nitride heterostructures. The synergy between the two institutions establishes a close working relationship leading to the synthesis of controlled diamond materials and their use in high-power devices.

15. SUBJECT TERMS
diamond, hexagonal/cubic boron nitride, interface characterization, surface modification, DFT/MD simulations, adhesion energy

16. SECURITY CLASSIFICATION OF:			**17. LIMITATION OF ABSTRACT**	**18. NUMBER OF PAGES**	**19a. NAME OF RESPONSIBLE PERSON**
					A Glen Birdwell
a. REPORT	**b. ABSTRACT**	**c. THIS PAGE**			**19b. TELEPHONE NUMBER (Include area code)**
Unclassified	Unclassified	Unclassified	UU	74	(301) 394-0601

Standard Form 298 (Rev. 8/98)
Prescribed by ANSI Std. Z39.18

Contents

List of Figures v

List of Tables ix

Acknowledgments x

1. Introduction 1

2. Events 2

3. Setup of State-of-the-Art Facilities for Fabrication of Diamond Single Crystals and Heterostructures 3

4. Materials of Interest and Growth Approaches 4

4.1 Growth and Preparation of h-BN–Diamond Heterostructures 4

4.2 Growth of Single-Crystalline and Polycrystalline Diamond by MPCVD 8

4.3 Growth for BN Thin Films by PLD and Optimization 14

4.3.1 Thin-Film Growth Method (PLD) 16

4.3.2 Target and Substrates Characterizations 18

4.3.3 BN Thin-Film Growth by PLD 20

5. State-of-the-Art Metrology Approaches Development of Characterization Techniques for Diamond–BN and Diamond–FET Interfaces 31

5.1 FIB Milling: Preparation of TEM Specimen from Bulk Structures 31

5.2 Aberration-Corrected Electron Microscopy: Microstructure and Interfaces 33

5.3 Diamond-Based FET (E46) Characterization 35

5.4 Other Metrology Approaches 39

5.4.1 THz Spectroscopy: Electrical and Electronic Properties of H-Terminated Diamond 39

5.4.2 Cyclotron Resonance Measurements: Carrier Effective Mass Calculations 40

5.4.3 Ellipsometry: Film Thickness, Roughness, and Optical Constants 42

6. Diamond Surface Modification and Doping: Amine, Amene, and Bromination of Diamond Surfaces 44

7. Theoretical Studies Performed with Classical and Quantum Theory Levels 47

7.1 Adhesion Energy Estimates of Diamond–BN Structures 47

7.2 Interfacial Energy Estimates for c-BN Grown on Diamond Surfaces 49

8. Collaborations between the Rice Team and DEVCOM ARL Team 50

9. Conclusions 51

10. References 54

List of Symbols, Abbreviations, and Acronyms 58

Distribution List 62

List of Figures

Fig. 1 Timeline for the establishment of Rice University National Security Research Accelerator in Dell Butcher Hall. This includes a state-of-the-art diamond growth facility for characterization. 3

Fig. 2 Diamond growth microwave-plasma CVD (MPCVD) systems, PLASSYS SSDR-150 (top left) and SEKI SDS6350 (bottom left), have been installed at the facility. (top right) The gas safety cabinets for H_2, methane (CH_4), and ammonia storage. (bottom right) The Pioneer 180 PLD equipment and the COMPEx 205 excimer laser. 4

Fig. 3 Schematic of the process for fabricating h-BN–diamond heterostructures 5

Fig. 4 a) SEM image of h-BN on Cu film. b) Optical image of h-BN transferred on SiO_2–Si. c) Raman spectra showing the E_{2g} peak of h-BN. d) AFM image and e) height reveal the thickness of the film is 2 nm. 6

Fig. 5 a) Schematic of the process for transferring h-BN onto E117. b) Image of E117 in XPS chamber. XPS measurements were performed on the red spots. c) XPS survey spectra of all the measured spots. 7

Fig. 6 a) Cross-sectional TEM image of h-BN on diamond. b) AFM image and height profile of the same h-BN film on SiO_2–Si. 7

Fig. 7 Schematic of the protocol for diamond growth and characterizations . 8

Fig. 8 Photos of a) a 2-inch PCD on Si wafer and b) the ongoing growth inside the chamber. c, d) SEM images of PCD. Raman spectra of e) Rice-grown PCD and f) Element Six PCD. 9

Fig. 9 a) Various nanodiamond seeds solutions. b) XRD patterns of PCD grown on Si (111) and Si (110). The influence of c) CH_4:H_2 ratio and d) average growth temperature on the growth rate. 10

Fig. 10 Photos of PCD films with a) the Rice owl pattern and b) ARL-Rice logos. c) Raman spectra of PCD inside and outside the pattern. d) Optical image and e) SEM image of the boundary of the pattern. 11

Fig. 11 Photos of a) HPHT diamond seed, b) ongoing SCD growth inside the chamber, and c) SCD after growth. d) Raman spectra and e) XPS spectra of the as-grown SCD and HPHT seed. f) Optical image and SEM image of as-grown SCD surface. 11

Fig. 12 Raman spectra of thick SCDs and their seeds 12

Fig. 13 Photos of a thin SCD grown on a diamond seed a) on a Mo disk and b) without the Mo disk. c) Optical image of the SCD surface. d) Raman spectra and e) XRD patterns of SCD4 and the seed. 12

Fig. 14 XPS survey spectra and Si 2p spectra of a) as-received E6 SCD, b) acid-cleaned E6 SCD, and c) the same SCD after HF/HNO_3 dip....... 13

Fig. 15 XPS spectra collected on the SCD5 surface 13

Fig. 16 UWBG and wide-bandgap semiconductors with their potential device performances. a) BFOM for various conventional wide-bandgap and UWBG semiconductors and b) FET schematics made of n-type c-BN and p-type diamond.. 14

Fig. 17 Structure and growth of BN. a) Phase transformation from h-BN to c-BN at high-temperature and pressure. b) Formation of a-BN, h-BN, and nanocrystalline c-BN... 16

Fig. 18 PLD: a) schematic of a typical PLD process where a pulsed laser hits the target surface generating plasma that then goes to the substrate and deposits to form a film, b) PLD facility installed at Rice with real-time plasma formation during the growth, and c) typical images of BN films grown on different substrates.. 17

Fig. 19 a) Typical Ar^+ ion-beam source and b) its operation during the growth 18

Fig. 20 Characterization of target for laser ablation. a) XRD pattern and b) B 1s and c) N 1s core XPS show the target is of h-BN nature with the presence of both B and N in approximately 1:1 elemental ratio. Inset shows the image of a commercial BN target. 19

Fig. 21 Characterization of substrates used for BN thin-film deposition. (Upper panel) *c*-Al_2O_3 and (lower panel) diamond. XRD, rocking curve, AFM topography, and substrate images of a–c) *c*-Al_2O_3 and d–f) SCD. 20

Fig. 22 Optimization of growth parameters for BN–Al_2O_3 film growth. Elemental B 1s and N 1s core XPS of BN films: a) growth-temperature dependent, b) growth-pressure dependent, and c) thickness dependent. 21

Fig. 23 Characterizations of BN–Al_2O_3 films: thickness-dependent a) AFM (clockwise), b) FTIR, and (c) Raman spectra of films 22

Fig. 24 Optimization of BN thin-film growth: a, b) repetition-rate-dependent surface morphology and corresponding XPS and c, d) ion-beam-assisted growth morphology and corresponding XPS 23

Fig. 25 Optimization of BN films growth. Comparative surface morphology of a) as-grown film and keeping the same N_2 growth pressure while cooling, and b) keeping the film at same growth-temperature and pressure for approximately 3 h after the growth. In all cases, we provided the same number of laser shots for BN growth. 24

Fig. 26 Properties of BN–Al_2O_3 thin films. a) UV-visible absorbance and b) magnetization measurements showing the UWBG nature and nonmagnetic behavior. Inset shows the transparent nature of the film. 25

Fig. 27 Characterizations of BN–GaN films: a) elemental XPS scans, b) FTIR, and c) Raman spectra showing the growth of BN. Inset shows the AFM image of the film. 26

Fig. 28 Cross-sectional atomically resolved STEM images of the BN–GaN film. a) Grown GaN by MOCVD and b) BN layer grown by PLD. c) Energy dispersive X-ray (EDS) analysis mapping shows the uniform presence of B and N, and d) EELS mapping confirms the presence of B and N. 27

Fig. 29 Spatial SHG of BN–GaN film: a) Intensity mapping and b) the probability vs. photon intensity count showing that the film is SHC active 28

Fig. 30 Characterizations of BN–PCD films: a) XPS at B 1s and N 1s core of as-grown and in-situ 3-h annealed BN–PCD films and b) corresponding AFM surface topography 29

Fig. 31 Comparative XPS of BN–PCD films. Films were grown on a) home-grown PCD and b) commercially purchased PCD from Element Six. 29

Fig. 32 XPS of BN film grown on normal-grade SCD: a) B 1s, b) N 1s, and c) C 1s cores 30

Fig. 33 Characterizations of BN–SCD films: a) XRD azimuthal symmetry phi-scan, b) AFM surface topography, and c) Raman spectra of a BN–SCD film 30

Fig. 34 Cross-sectional HRTEM images of BN–SCD films. a) As-grown and b) in-situ 4-h annealed film at the same growth temperature and pressure, showing the formation of a dense BN layer in between of diamond and Au. 31

Fig. 35 Schematic of a FIB unit (middle) consisting of an electron beam, ion beam, metal and C gas source, and an easy needle for specimen movement (lift out). Step 1: Sputtering of a conductive protection layer. Step 2: Bulk cut followed by U cut. Step 3: Easy needle attachment. Step 4: Lift off the specimen from the surface. Step 5: Attachment of the specimen to the TEM half-grid post. Step 6: Polishing the specimen up to a thickness level of less than 100 nm... 32

Fig. 36 (Left) FIB-prepared TEM specimen; (middle) schematic showing the bright field, dark field, EDS, and EELS; and (right) corresponding microscopy images and EELS spectrum for CVD-grown SCD 33

Fig. 37 Schematic of transfer-doped diamond FET, where the crystallographic quality of source and drain diamond channel interface need to be crystallographically intact and free from impurities and defects. Similarly, the gate dielectric and channel interface must ensure homogenous distribution of the transfer dopant as well (here it uses V_2O_5). Various interfaces of interest are flagged by red-patterned boxes. 34

Fig. 38 (Top to bottom) The 100-nm thin layer of diamond grown on SCD wafer, PLD-deposited h-BN layer on electronic-grade SCD wafer, metal oxide–h-BN–SCD structures, PLD-deposited c-BN on electronic-grade diamond, and finally, the B ion–implanted single crystalline wafers. Various interfaces of interest are flagged by red-patterned boxes. 35

Fig. 39 Image of the E46 wafer with transistors of interest and pads flagged with the dotted rounded box (middle). (left) Top view of the pad (TLM #6) and (right) top and cross-sectional views of the transistor (E46-P-9). 36

Fig. 40 (Left) (100) surface of electronic-grade SCD. (middle) Cross-sectional schematic image of diamond transistor and corresponding low-magnification STEM image. (Right) Channel-gate dielectric-gate electrode interface. (Bottom) Moderately magnified images: (from left to right) source-channel interface, source-diamond-channel interface, transfer dopant-channel-diamond interface, diamond-gate dielectric-gate electrode interface, diamond-channel-transfer dopant interface, and source-channel diamond interface........ 37

Fig. 41 Inference: the source contact–diamond interface is atomically sharp and crystallographically intact and free from any defects 37

Fig. 42 Inference: the metal oxide V_2O_5–diamond interface is 99% homogenous with some metal oxide deterioration due to the exposure of lamella to atmospheric moisture during the transfer from the FIB chamber to the TEM CompuStage........ 38

Fig. 43 Inference: as expected, an amorphous metal oxide layer, Al_2O_3, is present between the gate channel interface and a bubble-like vacuum area produced by the presence of trapped air bubble during the fabrication process and can also be seen in the high-magnification image........ 38

Fig. 44 (left) Real (top) and imaginary (bottom) conductivity values of H-polycrystalline and single crystalline wafers calculated through THs-TDS measurements. (right) Comparison between conductivity values measured using THz and conventional van der Pauw probe measurement. Conductivity values computed are comparable......... 40

Fig. 45 The CR signal from an H-terminated SCD wafer is very feeble and found to have no change in the frequency range with respect to the applied magnetic field. This implies either the mobility of free carriers is too low, or under vacuum or humidity-free conditions, the carrier density is too low due to the lack of atmospheric transfer doping species. 41

Fig. 46 (Left) Primary tools for collecting ellipsometry data: light source, polarization generator, sample, polarization analyzer, and detector. (Right) Flowchart showing the common procedure used to deduce material properties from ellipsometry measurements, which is basically a regression analysis as an exact equation describing the sample cannot be written. (Image courtesy of J.A. Woollam Ellipsometry Solutions.) 43

Fig. 47 (Left) Schematic illustration of the H- and O-terminated (100) diamond surfaces and (right) the formation of surface dipoles at H- and O-terminated diamond surfaces due to the difference in the electronegativity between C, H, and O. 44

Fig. 48 Information on the functional groups resultant from different treatments as revealed by ATR–FTIR spectroscopy: a) N concentration of the samples b) with and c) without the HBr treatment, calculated from high-resolution XPS. The ratio of N-related groups d) in aminated samples, resolved from XPS N 1s core, and the morphology of e) pristine BDD and f) aminated BDD by SEM. 47

Fig. 49 Example of the models used to evaluate the adhesion energy, E_{AE}: an h-BN sheet on a hydrogenated diamond (001) face and c-BN on a bare diamond (001) face. For c-BN, there are two possibilities: c-BN face rich in either B or N atoms in contact with the diamond surface. 48

Fig. 50 h-BN–diamond and c-BN–diamond heterostructures used to estimate the interfacial energy, E_{int} 49

List of Tables

Table 1 Comparative properties of c-BN and diamond 15

Table 2 Adhesion energy between h-BN and c-BN on bare and H-terminated diamond surfaces 48

Table 3 Theoretical interfacial bond length, $E_{AE,}$ and E_{int} for c-BN–diamond heterostructures 50

Table 4 Samples exchanging between Rice and DEVCOM ARL.................. 51

Acknowledgments

The following people were involved and are thanked:

- Rice University: Dr Pulickel Ajayan, Dr Robert Vajtai, Dr Xiang Zhang, Dr Anand B Puthirath, Dr Abhijit Biswas, Dr Eliezer Oliveira, Chenxi Li, Harikishan Kannan, and Tia Gray
- DEVCOM ARL: Dr Tony Ivanov, Dr A Glen Birdwell, Dr Dmitry Ruzmetov, Dr Mahesh Neupane, Dr Pankaj Shah, Dr Sergey Rudin, James Weil, Leonard De La Cruz, Derwin Washington, and Stephen B Kelley
- Naval Research Laboratory: Dr Bradford B Pate
- Collaborators: Dr Di Chen (University of Houston), Dr Hanyu Zhu (Rice), Dr Aditya Mohite (Rice), and Dr Junichiro Kono (Rice)

1. Introduction

With the increasing demand for silicon (Si) electronics in terms of power and energy considerations, wide-bandgap semiconductors have become a viable option, enabling new device architectures and the use of new semiconductor materials.[1] Among these, silicon carbide (SiC)- and gallium nitride (GaN)-based devices have been explored widely.[2–4] However, it has been realized recently that diamond, an ultra-wide-bandgap (UWBG) (>5 eV) material, has significant advantages compared with GaN or SiC if implemented in high-power devices.[5] Owing to the ultra-high bandgap and extremely high thermal conductivity, diamond has been touted as the next-generation material for high-voltage, high-power, high-temperature, and high-frequency devices.[6] The band structure in hydrogenated diamond allows it to act as easy electron emitters to vacuum levels, at higher voltages, which can be captured in a dielectric layer placed on top of the diamond, and in the process, also generate high hole conduction in the diamond layer.[7] Hence diamond, with the right kind of interface dielectric layer and doping, can become exciting building blocks for transistors and metal–oxide–semiconductor field-effect transistors (MOSFETs), the drivers of the semiconductor industry. The high thermal conductivity[8] of diamond also allows excellent intrinsic thermal management, so far a bottleneck with Si and other semiconductor device technologies.

The advantages aside, there are significant challenges ahead in realizing diamond-based device technologies. These are mainly related to the growth of high-quality diamond films, selection and adoption of the right interface dielectric layer, controlled doping to enable device polarity, and contact issues with metal lines. In recent years, various attempts have been made to address these issues and improve the performance of diamond devices. Recent advances in chemical vapor deposition (CVD)[9] of diamond have resulted in the ability to grow good-quality single- and polycrystalline films over areas ranging from a few millimeters to several centimeters.[10] For the dielectric layer over diamond, several metal–oxide films have been explored (e.g., alumina, molybdenum trioxide, and so on) with varying degrees of success based on the interface structure, epitaxy, and charges present. For the doping part, various approaches have enabled p- and n-type structures to be produced with dopants such as boron (B) and phosphorus (P).[11] However uniform and controlled doping has been extremely challenging leading to techniques that alter the diamond surface terminations (hydrogen [H] or oxygen [O]). These surface modifications, termed transfer doping, alter the bandgap and electronic structure of diamond and enable higher charge-carrier densities and mobilities, although the interface layer selection has to match the nature of transfer doping used.

The specific objectives of the project are the following:

- Establishing a CVD facility for the growth of large-area, high-quality diamond films, vapor-phase doping methods, and electronic and thermal characterization tools for the grown diamond films and diamond-based heterostructures.
- Developing and optimizing various approaches that would enable the synthesis of heteroepitaxial diamond–boron nitride (BN) heterostructures, including diamond–BN (hexagonal BN [h-BN] and cubic BN [c-BN]), diamond–hexagonal boron carbonitride (h-BCN), and other multilayer structures including the gate dielectric.
- Developing methods that would enable various types of doping of the diamond films to engineer their bandgap and electronic structure and understand the interface structural and electronic properties of the doped diamond films and BN layers.
- Engineering electrical contacts between diamond–BN–dielectric films and a selection of metals and alloys, and integrating and testing these in field-effect transistor (FET) diamond devices.
- Developing close collaborations with the US Army Combat Capabilities Development Command Army Research Laboratory to develop electronic device architectures for the diamond–BN heterostructures grown at Rice University, and fabricating and testing these devices both at Rice and the DEVCOM Army Research Laboratory. The goal will be to achieve far better device performance compared to existing diamond wide-bandgap devices, based on well-defined device metrics.
- Exploring, in subsequent years, novel applications, outside of semiconductor device applications, for the diamond–BN heterostructures such as quantum sensing, single-photon emission, thermal management, and optoelectronics.

2. Events

- Materials Research Society Fall Meeting, Diamond Electronics, 12/1/2020–12/2/2020, online
- The 6-month review meeting, 5/3/2021, online
- DEVCOM ARL director's visit, 9/30/2021, Rice University
- The annual review meeting, 12/1/2021, online

- Biweekly meeting, 11/6/2020 to present, online

3. Setup of State-of-the-Art Facilities for Fabrication of Diamond Single Crystals and Heterostructures

Rice invested a substantial amount of funds and energy to establish the laboratory and related office space. In the process of selecting the location of the new lab from several options, premium space in Dell Butcher Hall has been renovated into the new diamond growth facility. The advantage of this choice is the environment; this building is on Rice campus, in the engineering quad, and close to the cleanroom, main characterization facilities, and peer labs. The newly established Welch Foundation Materials Center will also be located in the same building. The process from location selection to the creation of the state-of-the-art facility is illustrated in Fig. 1.

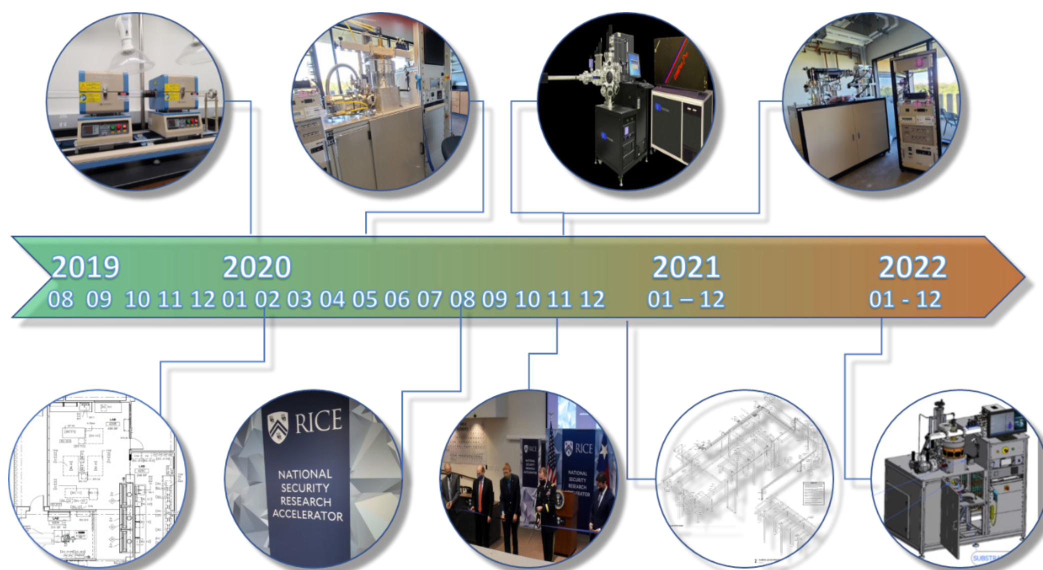

Fig. 1 Timeline for the establishment of Rice University National Security Research Accelerator in Dell Butcher Hall. This includes a state-of-the-art diamond growth facility for characterization.

Initially, the diamond substrates needed for research were purchased from the company Element Six. The goal is to transition to home-grown diamond substrates to better control the crystalline quality parameters, and during the last year, we were able to develop the start-synthesizing protocols for our home-grown diamond wafers, both single- and polycrystalline, with control over thickness, lateral size, and surface roughness.

At this point, most of the infrastructure at Rice is installed, and the diamond growth reactors and physical vapor deposition facilities have been commissioned.

Currently, the materials growth facility is running at full capacity, which includes two diamond growth reactors, PLASSYS SSDR-150 (MW 1.5–6 kW) and SEKI SDS6350 (MW 1.5–5 kW), and a pulsed laser deposition (PLD) system (a Pioneer 180 PLD chamber with an ion gun), a COMPEx 205 excimer laser, and finally, an ultra-high-purity gas handling system. A snapshots of the various facilities are depicted in Fig. 2.

Fig. 2 Diamond growth microwave-plasma CVD (MPCVD) systems, PLASSYS SSDR-150 (top left) and SEKI SDS6350 (bottom left), have been installed at the facility. (top right) The gas safety cabinets for H_2, methane (CH_4), and ammonia storage. (bottom right) The Pioneer 180 PLD equipment and the COMPEx 205 excimer laser.

In summary, the lab space has been renovated, and the construction and installation of the growth reactors and the gas supply system are finished. The large equipment purchased in year 1 have been acquired and installed, and all the equipment installed is fully functional and in use. Further equipment planned for subsequent years, contingent upon the availability of funds, are another diamond growth MPCVD chamber for B doping, a reflection high-energy electron diffraction (RHEED) device mounted on the PLD setup, an electrical probe station, and a diamond polishing facility.

4. Materials of Interest and Growth Approaches

4.1 Growth and Preparation of h-BN–Diamond Heterostructures

In the past 2 years, we have been optimizing the fabrication of h-BN–diamond heterostructures. The introduction, background, and research plans for the h-BN and h-BN–diamond heterostructures can be found in the first-year report.[12]

Figure 3 shows the main procedures of the fabrication process. A copper (Cu) film is first deposited on a c-plane single-crystal sapphire substrate. High-temperature annealing can make the Cu film become (111) orientated and an ideal substrate for h-BN growth by CVD method. After the growth, the h-BN film is transferred onto a diamond device using a hybrid transfer method. Finally, the poly(methyl methacrylate) (PMMA) layer is dissolved before electrical measurement. From the sapphire substrate to the h-BN–diamond heterostructure, the entire process takes a few days to complete. It is worth noting that the Rice team has received a lot of help from the DEVCOM ARL team in several steps of this process. For example, the Cu film deposition and electrical measurement were performed at DEVCOM ARL. The diamond device was also prepared at DEVCOM ARL and sent to Rice. It shows a close collaboration between the Rice and DEVCOM ARL teams.

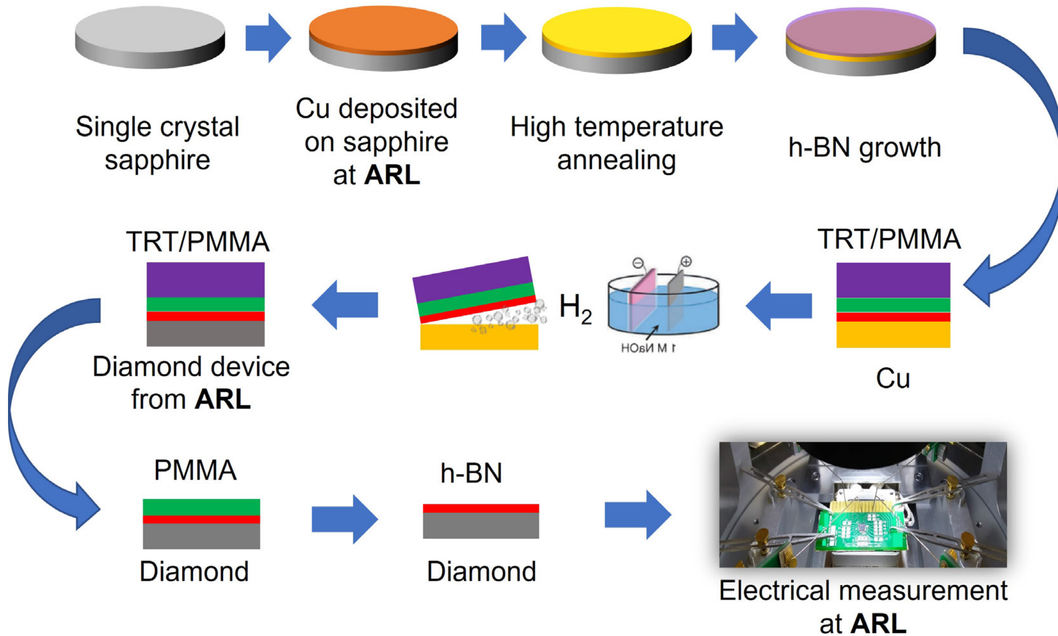

Fig. 3 Schematic of the process for fabricating h-BN–diamond heterostructures

Centimeter-large, high-quality h-BN films have been successfully synthesized on Cu films. The scanning electron microscopy (SEM) image of h-BN grown on a Cu film in Fig. 4a shows the high uniformity of the grown h-BN film. Before transferring the h-BN film onto diamond, we first transferred it to a silicon dioxide (SiO_2)–Si substrate for characterization, as display in Fig. 4b. The E_{2g} peak (~1369.8 cm^{-1}) of h-BN can be found in the Raman spectra in Fig. 4c. An atomic force microscopy (AFM) image (Fig. 4d) and height profile (Fig. 4e) reveal the film thickness is about 2 nm.

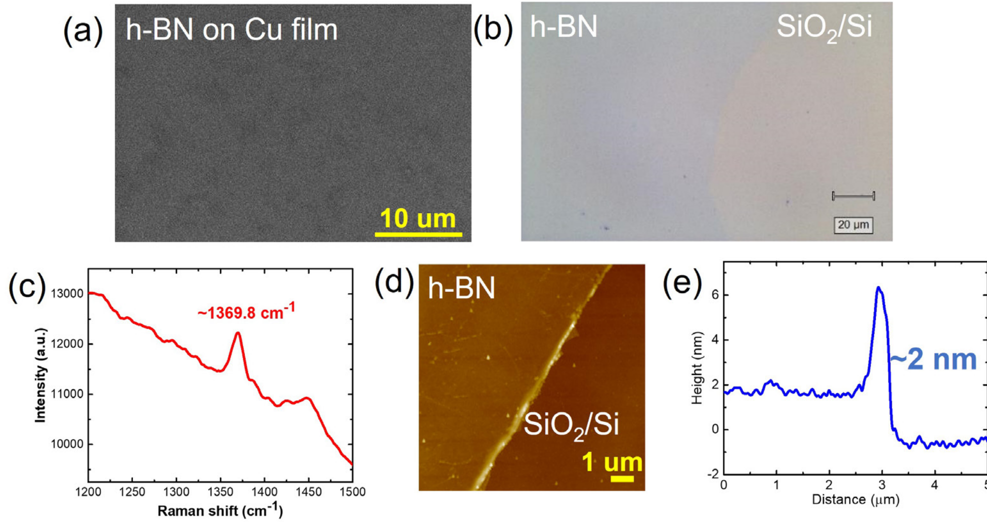

Fig. 4 a) SEM image of h-BN on Cu film. b) Optical image of h-BN transferred on SiO_2–Si. c) Raman spectra showing the E_{2g} peak of h-BN. d) AFM image and e) height reveal the thickness of the film is 2 nm.

Next, we transferred an h-BN film onto a diamond plate E117 received from DEVCOM ARL (Fig. 5a). The sample has a gold (Au) coating to protect the H terminations on the surface. After etching the Au, the h-BN was transferred within 1 min. After the transfer, X-ray photoelectron spectroscopy (XPS) measurement was performed on several spots on the surface. All of them show B and nitrogen (N) peaks, indicating that h-BN has been successfully transferred and covers the entire diamond surface. This sample was then sent to DEVCOM ARL for electrical measurement after the pre-anneal at 250 °C in vacuum and a 51-nm vanadium pentoxide (V_2O_5) deposition. The sheet resistance of E117 is found to be 4.2 kΩ/ϒ, which is lower than most diamond FETs. Besides, the carrier mobility 112 cm^2/V s is higher than another diamond sample, E101, which does not have h-BN and shows a carrier mobility of 81 cm^2/V s. The hole concentration of E117 and E101 are 1.3×10^{13} and 2.5×10^{13} cm^{-2}, respectively. We are currently preparing and measuring more samples to confirm these results.

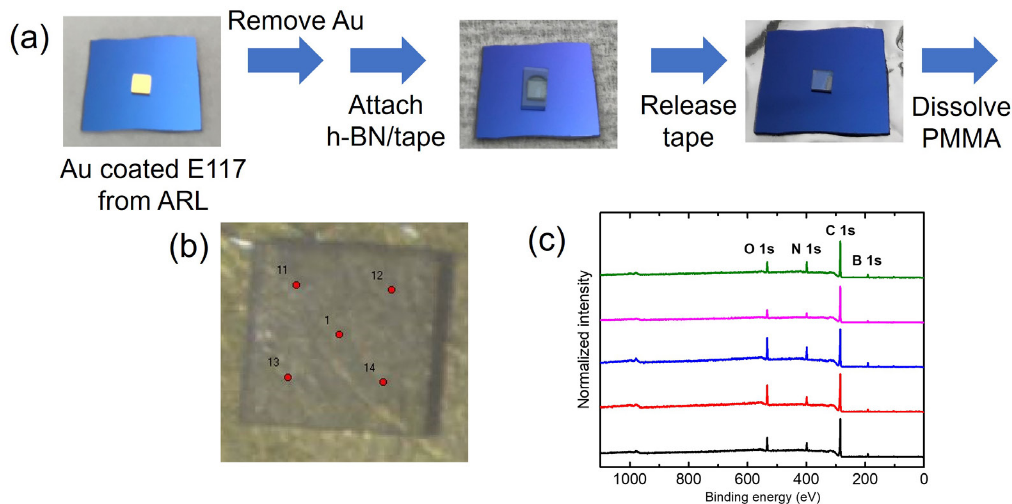

Fig. 5 a) Schematic of the process for transferring h-BN onto E117. b) Image of E117 in XPS chamber. XPS measurements were performed on the red spots. c) XPS survey spectra of all the measured spots.

In addition to growth and transfer, we also looked into the h-BN–diamond interface using focused ion beam (FIB) and transmission electron microscopy (TEM). As can be seen in Fig. 6a, the h-BN layers are sandwiched between Au and diamond. The h-BN–diamond interface is sharp and gapless. The number of layers of h-BN can be counted from the image, which is about 3–4 layers. This agrees well with the AFM measurement and height profile in Fig. 6b. All these results demonstrate the success of h-BN–diamond heterostructure fabrication.

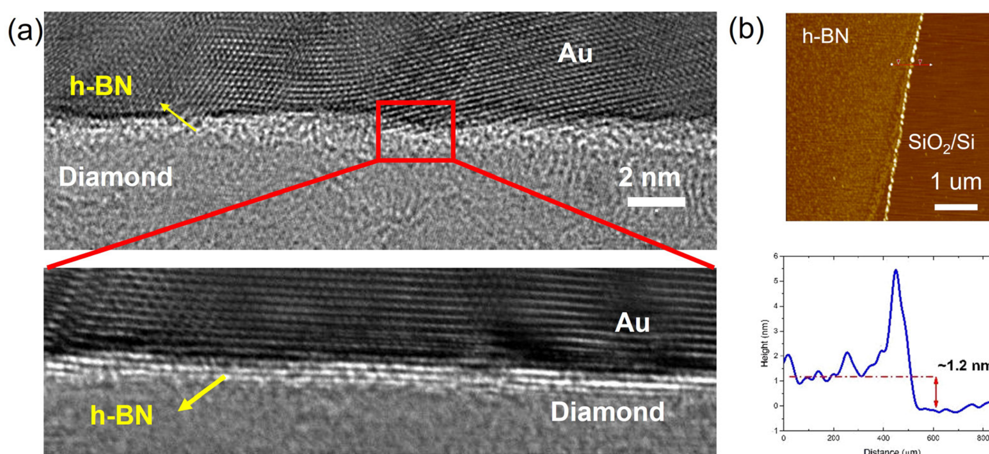

Fig. 6 a) Cross-sectional TEM image of h-BN on diamond. b) AFM image and height profile of the same h-BN film on SiO_2–Si.

4.2 Growth of Single-Crystalline and Polycrystalline Diamond by MPCVD

We started the diamond growth using the Plassys MPCVD system in March 2021 for single-crystalline diamond (SCD) and polycrystalline diamond (PCD). Due to the COVID pandemic, Plassys engineers could not come to the United States for installation and training. The Rice team managed to master the operations through online materials provided by the Plassys engineers. Despite the delay of the lab construction, we made temporary gas, chilling water, and exhaust connections to keep the chamber running until the end of September 2021 when the construction team began to finalize the gas piping.

A protocol (Fig. 7) for diamond growth and the following characterizations has been established. After we receive the diamond seed for SCD growth or an Si wafer for PCD growth, we first perform the acid cleaning, followed by the diamond growth in the MPCVD chamber. After growth, a series of characterizations is carried out to analyze the quality of the diamond, such as thickness measurement, Raman spectra, Fourier transform IR (FTIR) spectra, SEM imaging, XPS spectra, X-ray powder diffraction (XRD) patterns, TEM imaging, secondary ion mass spectrometry (SIMS) measurement, and so on. In addition, we also send the samples to DEVCOM ARL and other places for other measurements, such as electrical characterizations, thermal conductivity measurements, mechanical properties measurement, and so on.

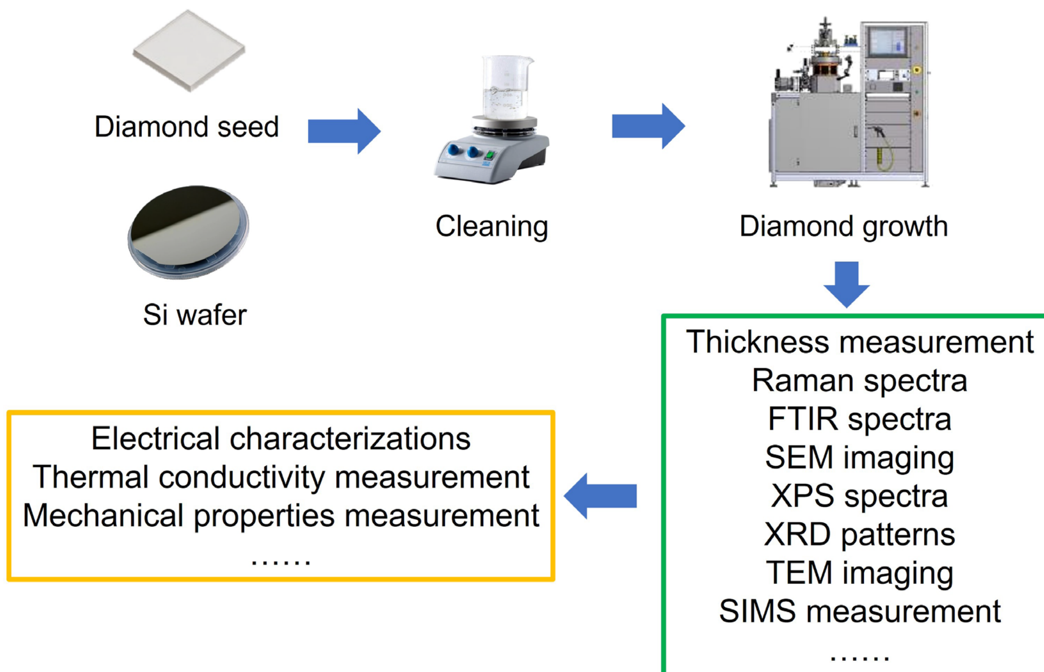

Fig. 7 Schematic of the protocol for diamond growth and characterizations

Figure 8 shows some results for PCD growth. We have successfully grown 2-inch PCD films on an Si wafer (Fig. 8a). Figure 8b shows a photo taken during growth, where a plasma plume covers the entire Si wafer. SEM images in Fig. 8c and 8d demonstrate the grain size of PCD is around 50 µm and the growth is along the vertical direction. The Raman spectra in Fig. 8e present a sharp diamond peak at around 1333 cm^{-1} with a narrow full width at half maximum (FWHM) of 2.96 cm^{-1}. No sp^2 carbon (C) peak or N peak can be observed. For comparison, the PCD from Element Six shows an FWHM of more than 7 cm^{-1} and a broad sp^2 C or N peak (Fig. 8f). These results indicate that our PCD film quality is much better than the quality of the Element Six PCD.

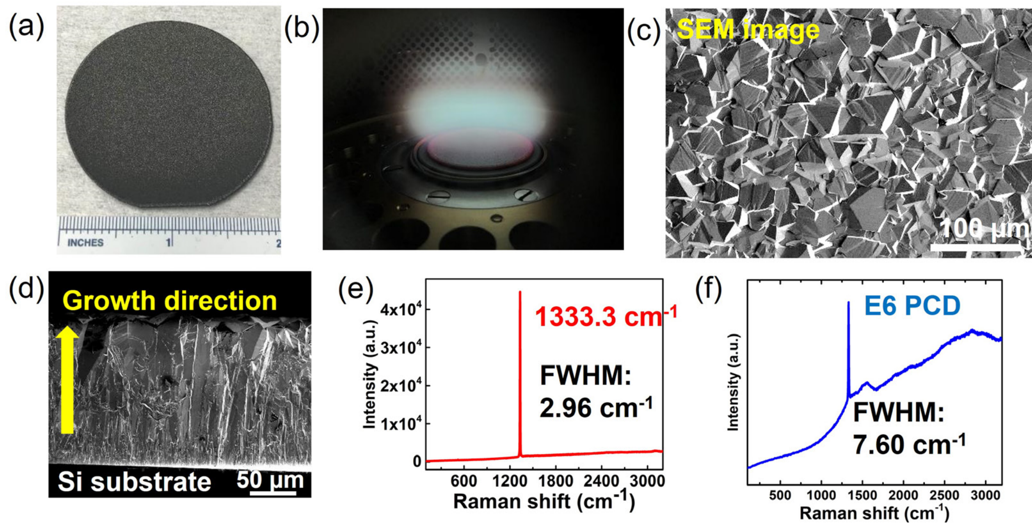

Fig. 8 Photos of a) a 2-inch PCD on Si wafer and b) the ongoing growth inside the chamber. c, d) SEM images of PCD. Raman spectra of e) Rice-grown PCD and f) Element Six PCD.

Several other topics related to PCD growth have been researched. For example, the influence of various nanodiamond seeds with different concentrations on PCD growth has been compared (Fig. 9a). The XRD patterns in Fig. 9b show the Si substrate orientation can affect the PCD orientation. While Si (100) leads to mainly (220) diamond growth, the growth on an Si (111) substrate shows more (111) facets than (220) and (311). Besides, the PCD growth rate is found to be largely influenced by the CH_4:H_2 ratio and growth temperature. The higher the CH_4:H_2 ratio or the higher the growth temperature, the higher the growth rate, as displayed in Fig. 9c and 9d, respectively.

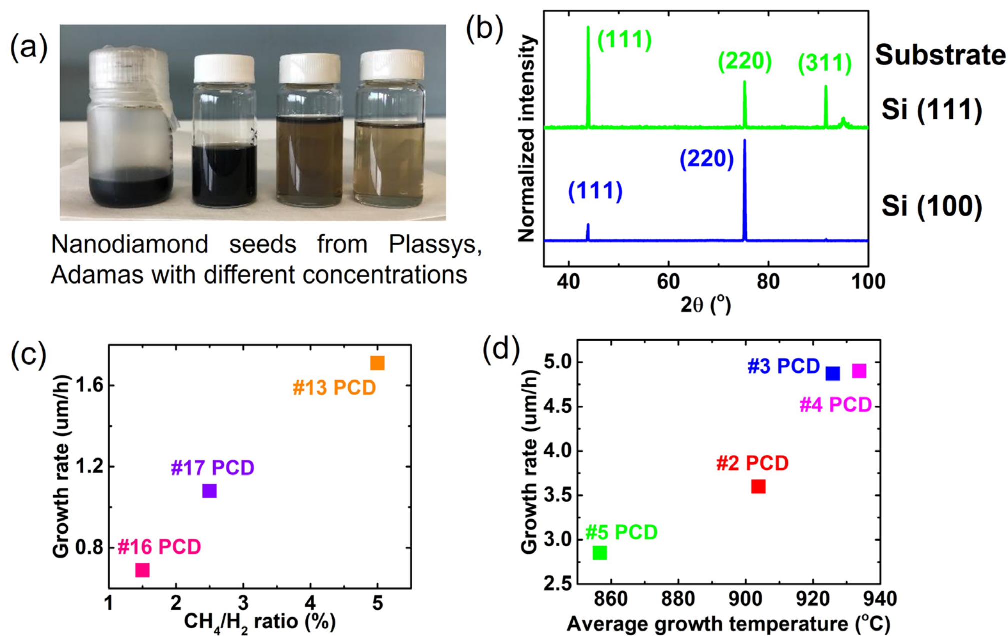

Fig. 9 a) Various nanodiamond seeds solutions. b) XRD patterns of PCD grown on Si (111) and Si (110). The influence of c) CH_4:H_2 ratio and d) average growth temperature on the growth rate.

Another interesting research topic we have been working on is diamond patterning. We received a task to make a diamond owl for visitors in only a few weeks, and thus developed a novel and simple method to create customized patterns on diamond. Figure 10a and 10b shows some examples, a diamond owl and DEVCOM ARL–Rice logos. The contrast of these patterns is caused by the different grain sizes, which are determined by the seeding method. While the Raman spectra in Fig. 10c indicate the inside and outside areas have similar Raman peaks, the boundary of these two areas with different grain sizes can be clearly observed in the optical image (Fig. 10d) and the SEM image (Fig. 10e).

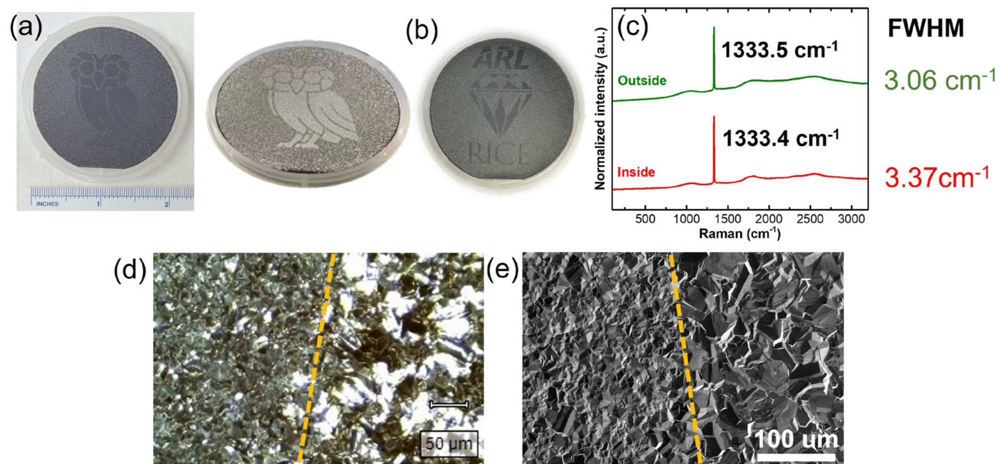

Fig. 10 Photos of PCD films with a) the Rice owl pattern and b) ARL–Rice logos. c) Raman spectra of PCD inside and outside the pattern. d) Optical image and e) SEM image of the boundary of the pattern.

The first SCD growth was performed on a high-pressure, high-temperature (HPHT) diamond seed, displayed in Fig. 11a–c. The thickness is about 0.589 mm. Figure 10d reveals the grown diamond presents nearly the same Raman peak as the seed. The XPS spectra in Fig. 11e demonstrates a high C peak with low O and Si peaks. Besides, the terrace structure can be observed on the surface, as shown in Fig. 11f.

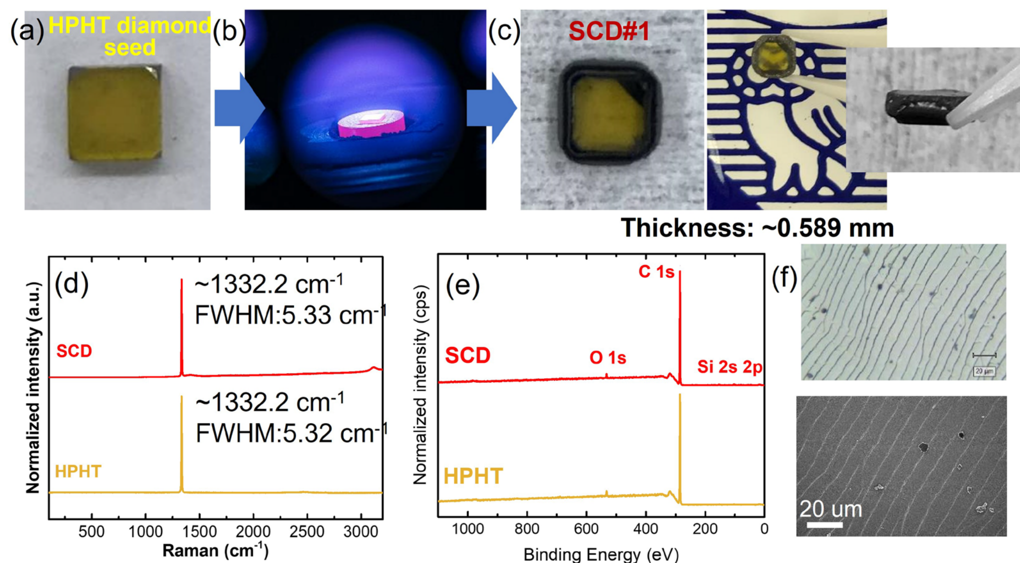

Fig. 11 Photos of a) HPHT diamond seed, b) ongoing SCD growth inside the chamber, and c) SCD after growth. d) Raman spectra and e) XPS spectra of the as-grown SCD and HPHT seed. f) Optical image and SEM image of as-grown SCD surface.

A few more thick diamond growths (SCD2 and SCD3) were carried out using HPHT seeds and Element Six SCD seed. The Raman spectra in Fig. 12a and 12b show that the FWHM becomes lower for the newer grown diamond, indicating that

the quality is improved after optimization. Besides, the diamond grown at Rice presents a lower FWHM compared to HPHT seed and Element Six SCD.

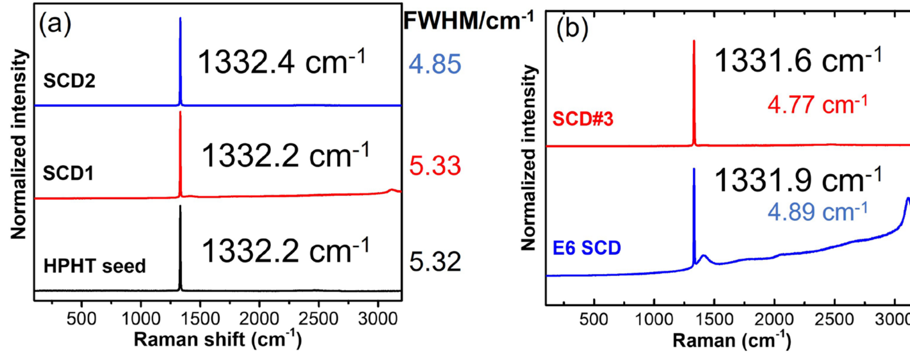

Fig. 12 Raman spectra of thick SCDs and their seeds

The SCD thin-film growth was also performed using Element Six SCD seed. The diamond film in Fig. 13a is about 15 µm thick, which can be lifted off by etching the molybdenum (Mo) disk (Fig. 13b). The optical image in Fig. 13c shows the surface is mostly flat and uniform. Figure 13d and 13e reveals that the Raman peak and XRD patterns of the grown diamond film and the seed are nearly the same.

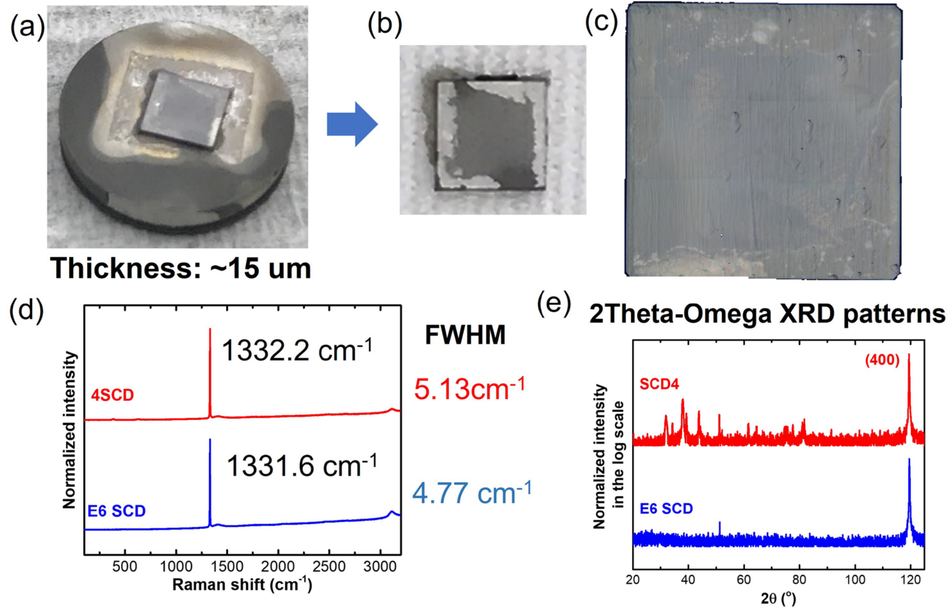

Fig. 13 Photos of a thin SCD grown on a diamond seed a) on a Mo disk and b) without the Mo disk. c) Optical image of the SCD surface. d) Raman spectra and e) XRD patterns of SCD4 and the seed.

We noticed that the concentration of Si on the as-received Element Six SCD is about 3.7% (Fig. 14a), which is quite high. After acid cleaning, the Si content can

be reduced to 1.8% (Fig. 14b). To further lower the Si concentration, we developed a new method using a hydrofluoric acid (HF)/nitric acid (HNO_3) dip. After the treatment, the Si concentration is only 0.4%, which is significantly reduced compared with the original Element Six SCD (Fig. 14c).

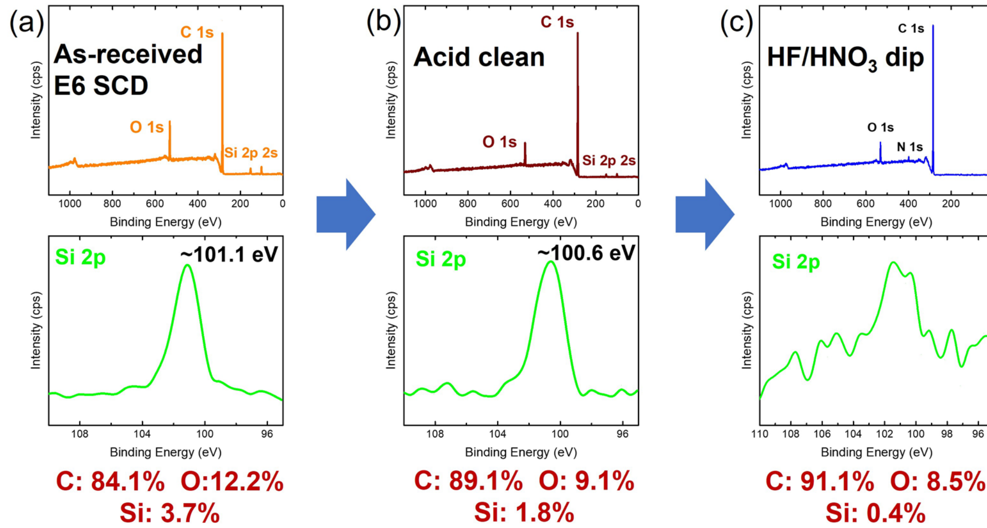

Fig. 14 XPS survey spectra and Si 2p spectra of a) as-received E6 SCD, b) acid-cleaned E6 SCD, and c) the same SCD after HF/HNO_3 dip

We further used this seed for growth. After optimizing the growth conditions, we can barely see any Si signal from XPS spectra in Fig. 15a. More XPS measurements were conducted on different spots. All of them show nearly 99% C, 1% O, and no Si (Fig. 15b). This shows that Si-free SCD growth has been achieved.

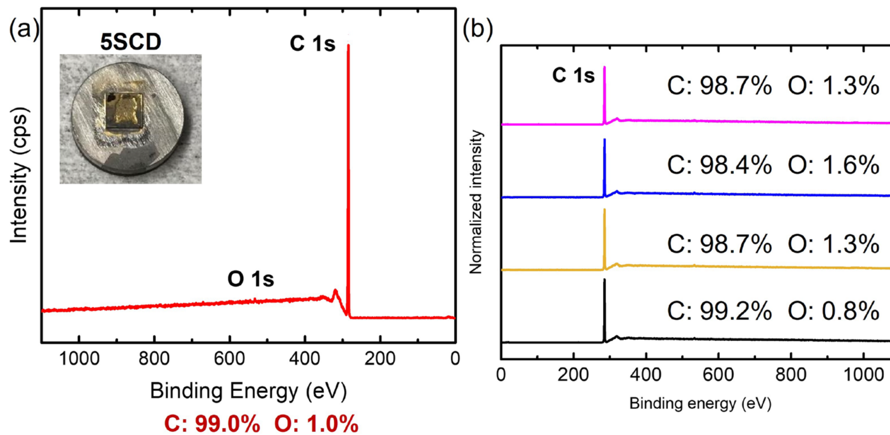

Fig. 15 XPS spectra collected on the SCD5 surface

4.3 Growth for BN Thin Films by PLD and Optimization

UWBG-based semiconductors lie at the heart of next-generation high-power and high-frequency electronic devices, owing to their high thermal, chemical, and mechanical stability. According to the Baliga figure of merit (BFOM) of power-loss (Fig. 16a), UWBG diamond and c-BN, the two hardest materials in the world, show great potential for an electronic device with a very high breakdown field (>10^7 V/cm) and less power loss.[13]

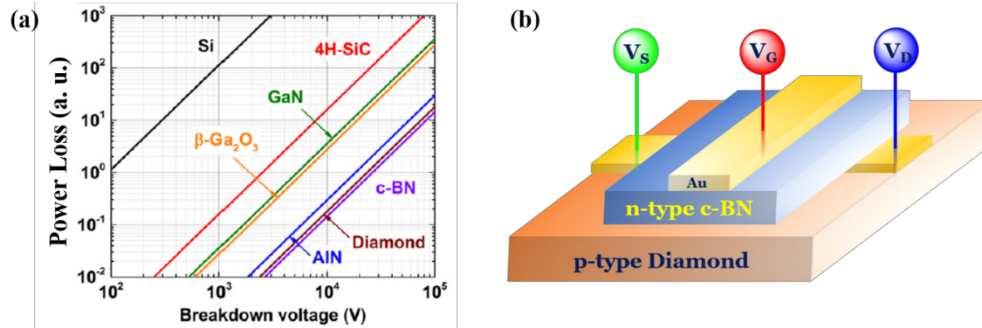

Fig. 16 UWBG and wide-bandgap semiconductors with their potential device performances. a) BFOM for various conventional wide-bandgap and UWBG semiconductors[13] and b) FET schematics made of n-type c-BN and p-type diamond.

Remarkably, both the diamond and c-BN are structurally, chemically, thermally, optically, and electronically compatible with each other. Their interesting properties are listed in Table 1. The only difference between them is that while c-BN can be made by both p- and n-type doping, diamond can only be made by p-type. Therefore, ideal high-mobility transistors could be made by forming the electronic-quality interfaces between the n-type c-BN and p-type diamond, forming the ultimate high-mobility FET device (Fig. 16b).[14]

Table 1 Comparative properties of c-BN and diamond[13]

Property	c-BN	Diamond
Lattice constant (Å)	3.61	3.56
Bond length (Å)	1.57	1.54
Bandgap (eV)	6.36	5.55
Density (gm/cm^3)	3.45	3.51
Density of atoms (m^{-3})	1.69×10^{29}	1.77×10^{29}
Hardness (kg/mm^2)	7500	10000
Stiffness (Young's modulus) (GPa)	700	1000
Refractive index	2.1	2.42
Thermal conductivity (W m^{-1}K^{-1})	1200	2000
Electrical resistivity (Ω-m)	10^8	10^9
Doping ability	Both p- and n-type	Only p-type
Oxidation resistance (°C)	>1200	>700
Corrosion resistance	Yes	Yes
BFOM (power loss in vertical device)	600	1100
Johnson figure of merit (power at high frequency)	8200	5800
Keyes figure of merit (for thermal limitation)	32	31

However, the growth of electronic-quality (highly oriented, single-crystalline, defect-free, large area, ultra-smooth) c-BN as well as diamond is the holy grail for the device scientists. Especially the growth of electronic-quality c-BN thin films not only on diamond, but also on any substrates by any growth methods still remains challenging, as B and N have a very rich and complex phase diagram, and depending on the pressure and temperature phase diagram, BN forms various phases (Fig. 17a).[15] The most stable form of BN is the hexagonal stacking of 2-D layers (h-BN). However, for device interest, our aim is to grow the cubic phase of BN (c-BN), which is metastable and can only be grown at very high temperature and pressure.

From a growth point of view, extensive efforts have been made for depositing c-BN thin films on various substrates (*c*-alumina/sapphire [Al_2O_3], Si, and diamond) by CVD, molecular beam epitaxy (MBE), and ion-beam-assisted PLD (IBAPLD), however, to little success. As shown, in most of the cases, it forms an interfacial defective BN layer (known as amorphous [a]-BN) during the film growth in order to release the interfacial energy (Fig. 17b).[16] Moreover, the interfaces were found to be abrupt, hindering it usefulness for high-performance devices as a lot of scattering centers form at the interface, reducing the carrier mobility. Therefore, one of the goals of our project is to grow electronic-quality c-BN–diamond heterostructures that have an atomically sharp, defect-free smooth interface in order to fabricate UWBG-based, high-performance FET devices.

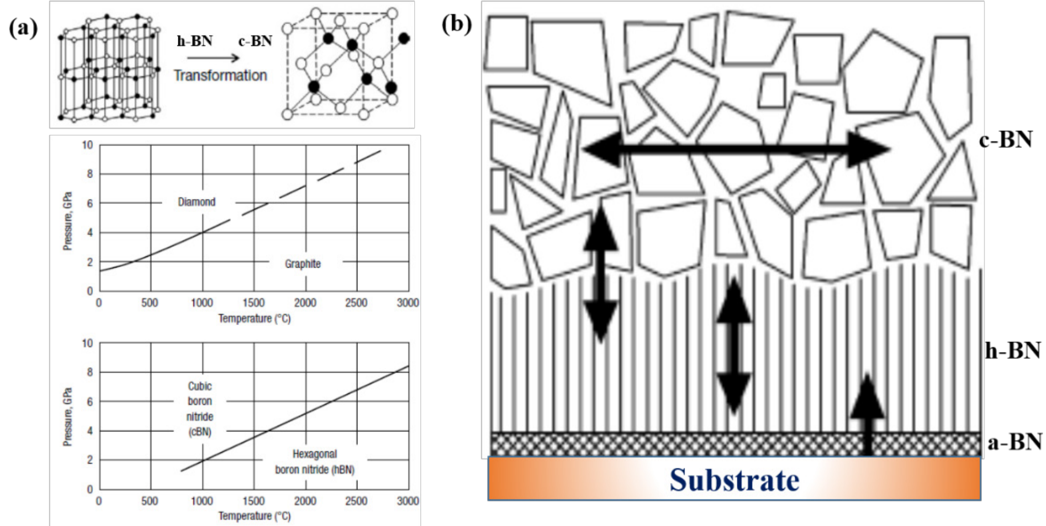

Fig. 17 Structure and growth of BN. a) Phase transformation from h-BN to c-BN at high-temperature and pressure. b) Formation of a-BN, h-BN, and nanocrystalline c-BN.[16]

4.3.1 Thin-Film Growth Method (PLD)

For c-BN thin-film growth, we adopted the highly energetic PLD process. In literature, most of the reported grown c-BN thin films are deposited by CVD or MBE methods, mostly forming turbostratic BN (t-BN) and mixed phase (h-BN + c-BN) films with disruptive interfaces, hindering its usefulness for high-performance devices by reducing the interfacial scattering. In addition, as stated in the literature, c-BN thin films can only be grown at very high temperature and pressure, thus requiring the additional supply of energy to B and N radicals during the growth. Therefore, we used a more advanced and ultra-clean, highly energetic, thermally nonequilibrium PLD process (Fig. 18a). The advantages of PLD over the other deposition processes is that a highly dense single- or polycrystalline target is ablated by a pulsed laser, in either high-vacuum or in the presence of the desired partial gas pressure, thus it is an ultra-clean growth process, leaving no residues on the film during deposition. In addition, importantly, it shows the faithful transfer of elements from the target onto the substrate surface in a stoichiometric ratio, which can grow in an epitaxial nature, depending on the film–substrate lattice mismatch endowed with the transfer of high-energy radicals and ions (energy ~10–100 eV) in the form of plasma, which travel to the substrate within few microseconds and *coalescence* on the substrate, resulting in the epilayer growth.[17]

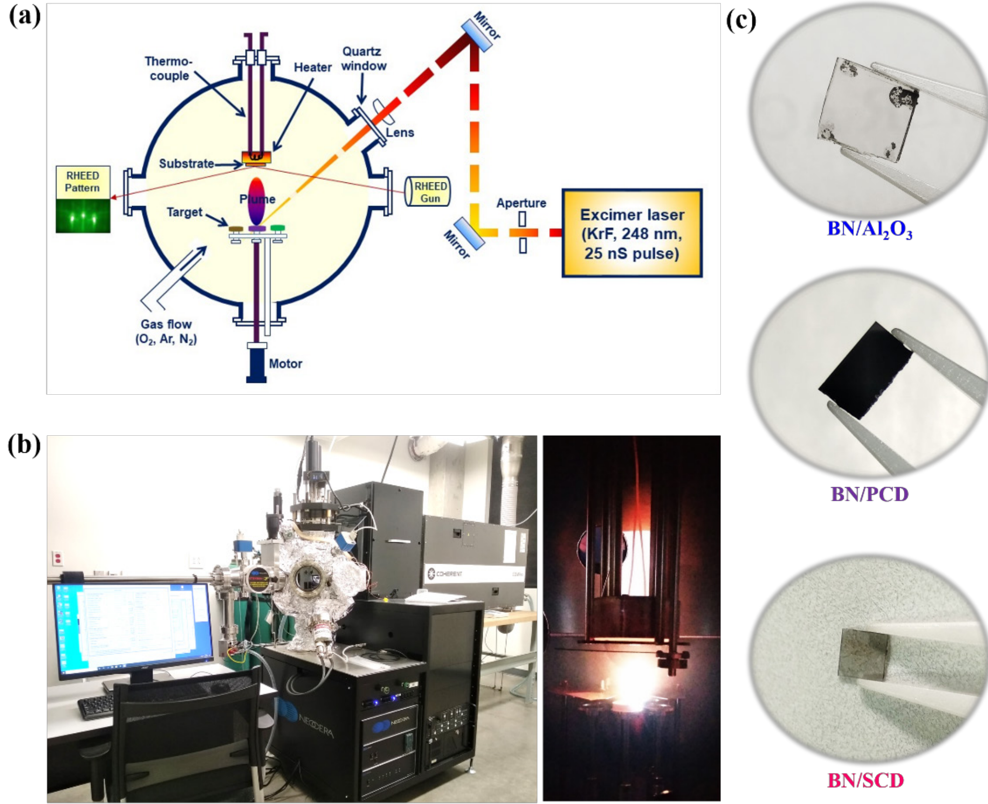

Fig. 18 PLD: a) schematic of a typical PLD process where a pulsed laser hits the target surface generating plasma that then goes to the substrate and deposits to form a film, b) PLD facility installed at Rice with real-time plasma formation during the growth, and c) typical images of BN films grown on different substrates

A typical advanced IBAPLD growth chamber (Pioneer 180 PLD) installed at Rice is shown along with the formation of plasma during the real-time BN thin-film growth (Fig. 18b). The krypton fluoride (KrF) excimer UV-laser has a wavelength of 248 nm (~5-eV photon energy) with a 25-nS pulsed width. The chamber is equipped with a substrate load-lock (load-lock vacuum, 5×10^{-8} Torr). It has a multi-target carousel with target rotation (maximum of six targets can be mounted at a given time for the multilayer growth) and target raster and software-controlled target selection, as needed, for multilayer and superlattice growth. The maximum vacuum of the chamber can go down to 2×10^{-9} Torr and the maximum achievable growth temperature is 800 °C. The typical maximum substrate size for the growth can be 10×10 mm^2. We generally use N partial pressure (10–100 mTorr) for the growth using mass flow controllers to provide the precise process pressure control. Additionally, our chamber is equipped with the ion-beam-assisted growth facility, where one can supply high-energy argon (Ar+) ions at high-acceleration voltage (300–800 V) to supply additional kinetic energy to the radicals, traveling toward the substrate (Fig. 19a). As an ion-beam source, Ar+ ions were generated by an RF

ion source. A typical Ar^+ ion-beam source and its operation during the growth are shown (Fig. 19b).

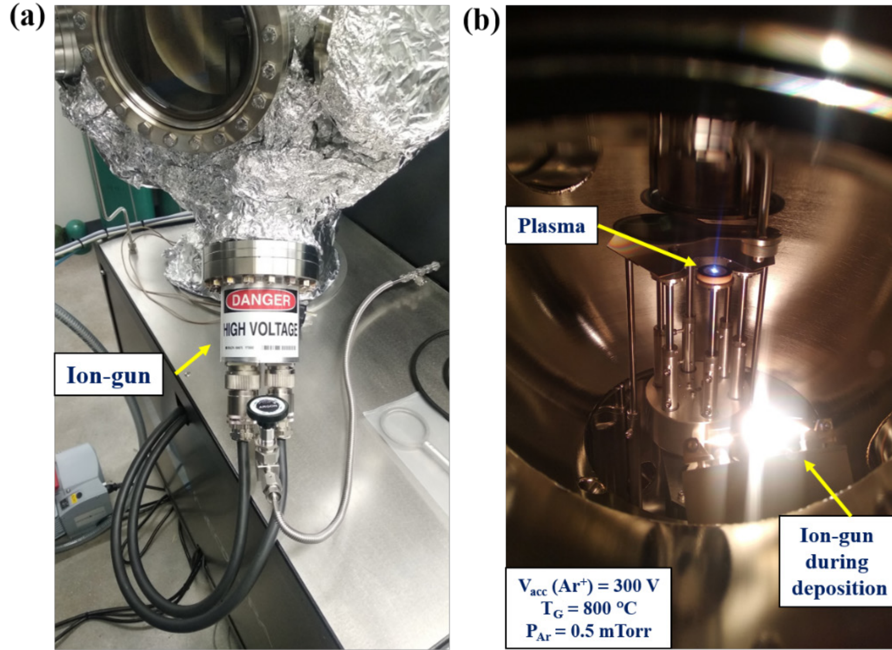

Fig. 19 a) Typical Ar^+ ion-beam source and b) its operation during the growth

Since various factors play crucial role during the film deposition, in order to obtain the high-quality thin films, one needs to optimize all the growth parameters (e.g., laser energy, pulse repetition rate, partial gas pressure, growth temperature, target-to-substrate distance, ablated spot size, and, of course, the quality of the substrate). For depositing BN films, we used *c*-Al_2O_3, GaN, and Element Six PCD and SCD substrates (both normal and electronic-grade) (Fig. 18c) and tried to optimize and understand the growth of BN films. The desired thickness of films is obtained by controlling the number of laser shots.

4.3.2 Target and Substrates Characterizations

For BN thin-film growth, we used a commercially available 1-inch-dense polycrystalline h-BN target (American Element, purity 99.9%) for laser ablation. To confirm the crystallinity and compositional ratio, we performed XRD of the target as well as XPS. From XRD, we can clearly see the polycrystalline nature of the target with the most intense (002) peak at approximately 26° (Fig. 20a). This show that the target is indeed of h-BN nature. Moreover, the elemental XPS scan shows the characteristic B–N bonds with an approximately 1:1 elemental ratio (42.5:50.5 to precious) (Fig. 20b and c).

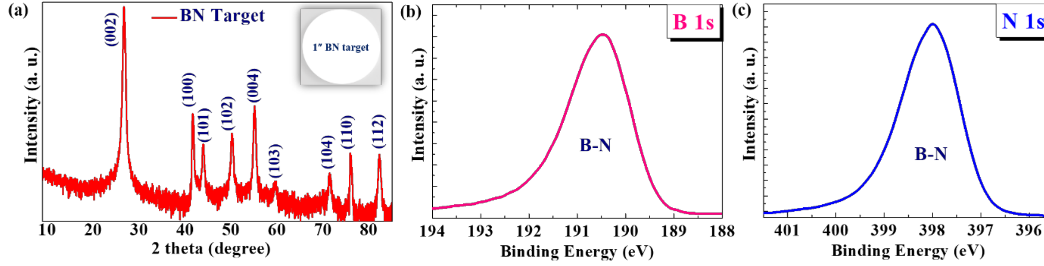

Fig. 20 Characterization of target for laser ablation. a) XRD pattern and b) B 1s and c) N 1s core XPS show the target is of h-BN nature with the presence of both B and N in approximately 1:1 elemental ratio. Inset shows the image of a commercial BN target.

We also characterized the commercially purchased *c*-Al_2O_3, PCD, and SCD substrates on which we deposited BN films (Fig. 21) (upper panel: *c*-Al_2O_3 and lower panel: diamond). XRD of both the sapphire and SCD shows highly oriented single-crystalline nature of the substrates, whereas PCD shows the presence of (111), (220), and (311) Bragg peaks in XRD (Fig. 21a and 21d). Importantly, we measured the miscut angle of the substrates (α), as it is important to understand the growth kinetics as well as the film–substrate interface quality. Miscut angle in commercially available substrates is unavoidable as it is limited by the crystal cutting tools. The miscut angle was measured by the difference between the rocking curve peak positions at 180° azimuthal angle difference, along the respective plane. As seen, sapphire shows very low miscut angle of approximately 0.089° along the A-plane and approximately 0.195° along the *m*-plane (Fig. 21b). On the other hand, SCD shows much higher miscut of more than 1° (Fig. 21e). Furthermore, AFM shows that the surfaces are flat, with a roughness of approximately 0.220 nm (for *c*-Al_2O_3) and approximately 0.225 nm (for SCD). The images of both (0001)-oriented sapphire and (001)-oriented SCD are also shown (Fig. 21c and 21f).

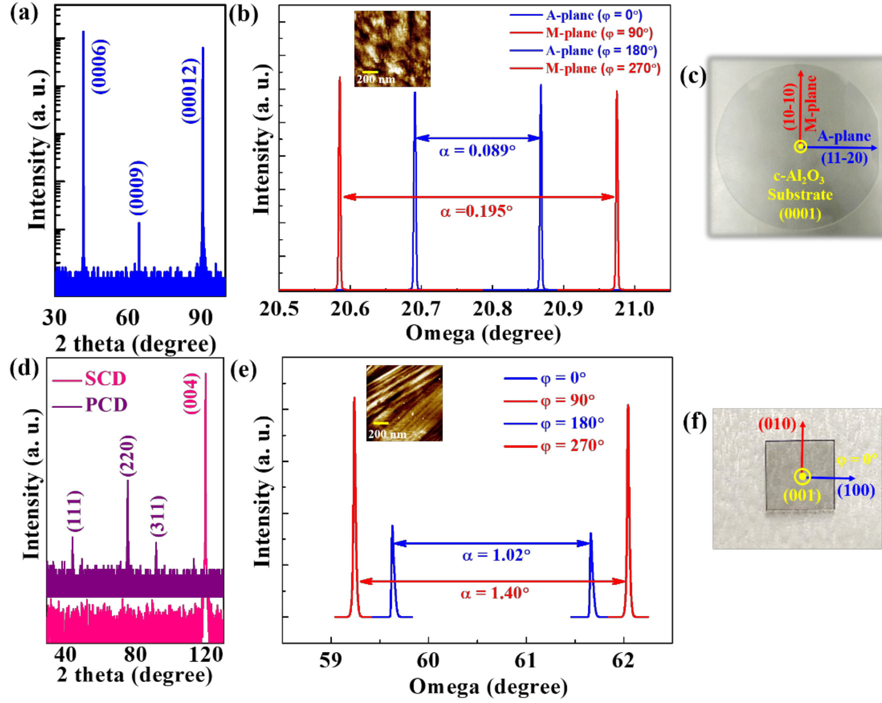

Fig. 21 Characterization of substrates used for BN thin-film deposition. (Upper panel) *c*-Al_2O_3 and (lower panel) diamond. XRD, rocking curve, AFM topography, and substrate images of a–c) *c*-Al_2O_3 and d–f) SCD.

4.3.3 BN Thin-Film Growth by PLD

4.3.3.1 BN–Sapphire Thin Films

First of all, we used (0001) *c*-plane sapphire substrates to optimize the BN thin-film growth. Structurally, sapphire forms a hexagonal corundum structure with lattice parameters of a = 4.75 Å and c = 12.99 Å. Interestingly, it is both structurally compatible to (0001) h-BN as well as along the (111) direction of c-BN. Since there is very little literature reported on BN thin-film growth by PLD, we first optimized the grown parameters by varying the growth temperature, pressure, repletion rate, and film thickness. While varying the growth temperature and pressure, we kept the film thickness the same (by using the same number of laser shots).

From XPS, as can be seen, for temperature-dependent films (having a film thickness of ~20 nm) and high-temperature growth, the films show the characteristic B–N bonding peak in XPS (Fig. 22a and b). However, when the film is grown at low temperature (e.g., at 200 °C), we observe a broad hump in B 1s core XPS, related with the B–O peak, possibly originating from the residual O inside the growth chamber as well as the ambient air oxidation effect. A similar situation occurs even when we vary the N partial pressure (P_{N2}) during growth (Fig. 22c and 22d). At a higher growth pressure, it shows clean XPS spectra, but

for films grown at lower pressure (e.g., 1 mTorr case), we observe a B–C hump, related to the carbonaceous surface contaminations. Therefore, from the growth temperature and pressure effects, we can clearly establish the fact that high-quality defect- and contaminant-free BN thin films can only be grown at HPHT conditions (e.g., T_G = 800 °C and P_{N2}= 100 mTorr).

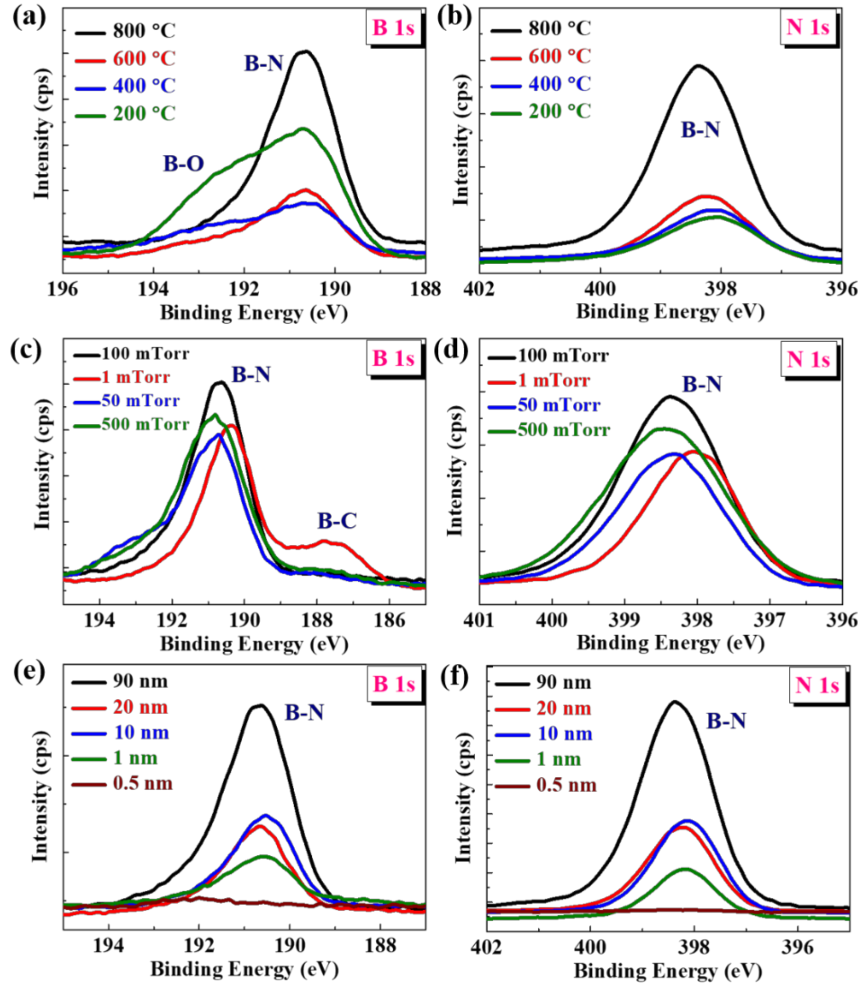

Fig. 22 Optimization of growth parameters for BN–Al_2O_3 film growth. Elemental B 1s and N 1s core XPS of BN films: a) growth-temperature dependent, b) growth-pressure dependent, and c) thickness dependent.

After knowing this fact, which is in accordance with literature reports, that BN can only be synthesized at HPHT conditions, we then tuned the film thickness by growing films under HPHT conditions and characterized them (Fig. 22e and 22f). As seen in XPS, film thickness was varied from thick to thin, typically from 90 nm to ultra-thin (~0.5 nm). Except for the ultra-thin film, all other films show the characteristic B–N peaks in XPS. From XPS, we also found an approximately 1:1 elemental ratio of B and N.

We performed surface topography of these films using AFM. As shown, the film surfaces were found to be smooth, and interestingly, it shows a triangular-shape island morphology with later sizes of 100–150 nm (Fig. 23a). Remarkably, these islands are unidirectional oriented, related to the growth kinetics and symmetry at the BN and sapphire interface. FTIR and Raman spectra show the peak at approximately 1360 cm^{-1}, confirming the growth of h-BN on sapphire (Fig. 23b and 23c). In addition, the low FWHM of the Raman peak of approximately 14 cm^{-1} (bulk BN of 5–7 cm^{-1}) also confirms the good crystalline quality of h-BN.

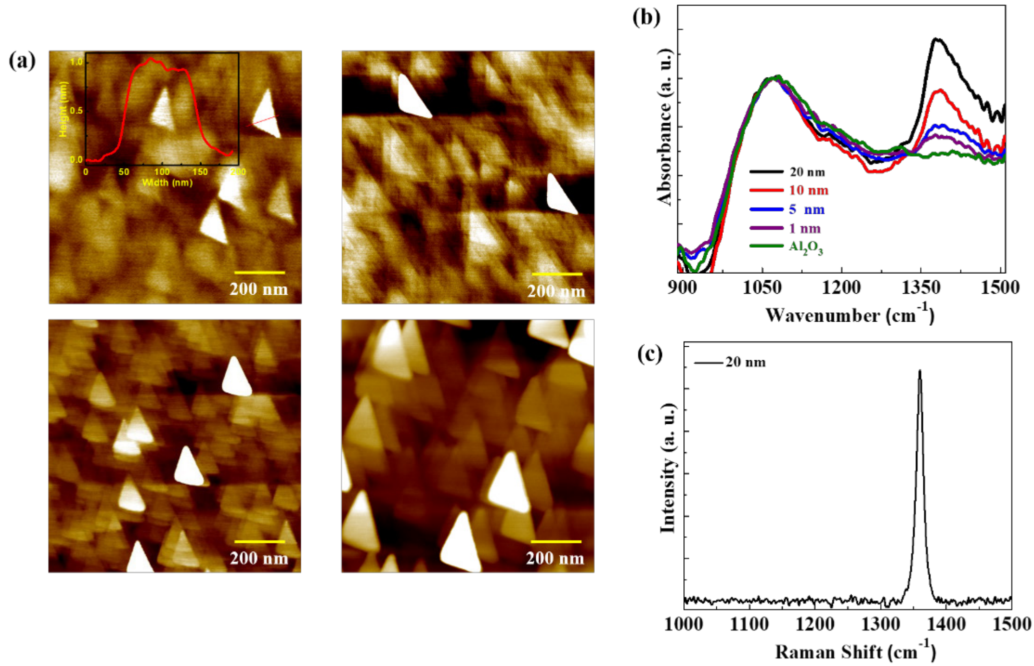

Fig. 23 Characterizations of BN–Al_2O_3 films: thickness-dependent a) AFM (clockwise), b) FTIR, and (c) Raman spectra of films

To understand and optimize the growth process further, we varied the repetition rate (i.e., number of laser pulses/second) to change the growth rate. Also, we used the ion beam during the deposition to supply extra kinetic energy during the growth; in some cases, IBPLD is also employed. Our growth chamber has an ion-beam-assisted deposition facility, where we can supply Ar+ ions with an acceleration voltage (V_{acc}) of 300 V while keeping the same growth temperature of 800 °C. However, the maximum N partial pressure can be supplied at 0.5 mTorr, which reduces the plume shape significantly. As observed, the growth morphology remains almost identical, even with the change in growth rate, suggesting that the growth rate has a negligible impact (Fig. 24a). However, we observed a significant change in the growth morphology when we used ion-beam-assisted deposition (Fig. 24b). It not only induces the C contamination, as shown in XPS (Fig. 24c and d) on the surface, but also reduces the island sizes significantly.

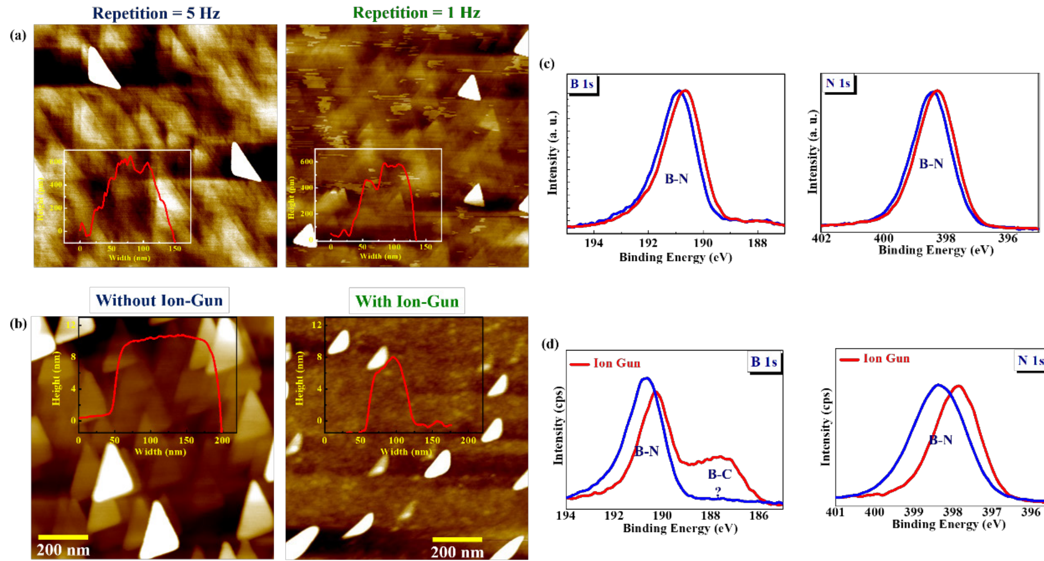

Fig. 24 Optimization of BN thin-film growth: a, b) repetition-rate-dependent surface morphology and corresponding XPS and c, d) ion-beam-assisted growth morphology and corresponding XPS

To increase the island sizes and thereby fully covering the surface with BN, we tried to in-situ anneal the film after growth. For one case, we kept the film at the same pressure and temperature for 3 h after growth, whereas for the other one, we supplied the same N_2 pressure while cooling the films (cooling rate of 20 °C/min). As can be seen, supplying only N_2 without the high-temperature annealing produces the 3-D island-like growth morphology (Fig. 25a). Remarkably, the high-temperature in-situ annealing slightly improves the island domain sizes (from 100 to 150 nm) (Fig. 25b). This again signifies that growth at high temperature is really a crucial factor for BN films. Considering all these optimizations, we can conclude that HPHT conditions are the most suitable for BN thin-film growth.

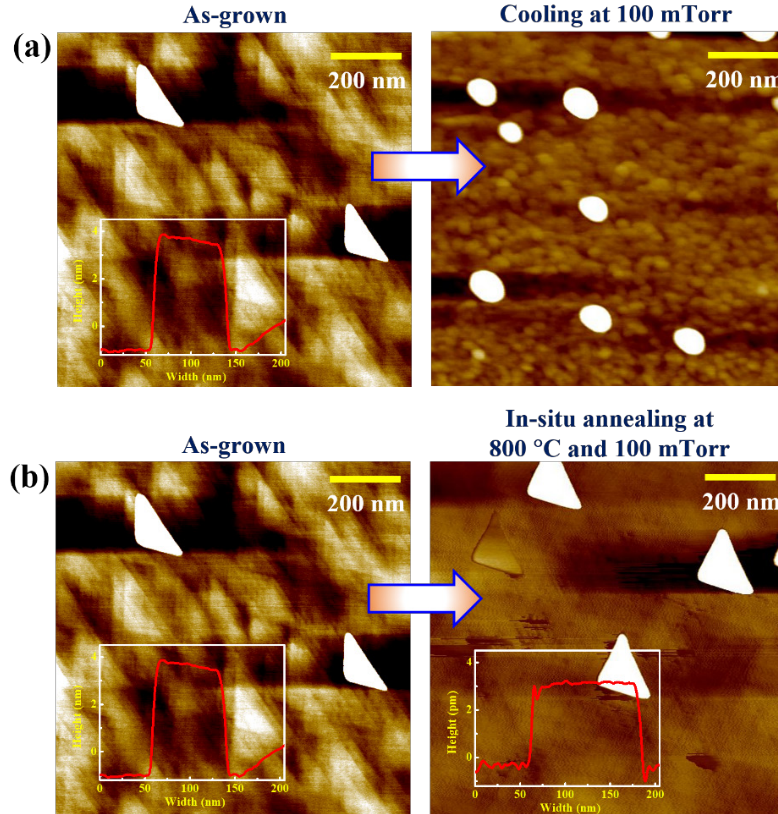

Fig. 25 Optimization of BN films growth. Comparative surface morphology of a) as-grown film and keeping the same N_2 growth pressure while cooling, and b) keeping the film at same growth-temperature and pressure for approximately 3 h after the growth. In all cases, we provided the same number of laser shots for BN growth.

Furthermore, we also measured the bandgap of the film as well as its magnetic characteristics. The UV-visible absorbance shows band tailing at approximately 214 nm and, from the corresponding Tauc plot, we obtained the direct bandgap of approximately 5.95 eV (Fig. 26a). Moreover, magnetic measurement shows the nonmagnetic behavior, consistent with the fact that pure phase, defect-free BN is nonmagnetic as none of the surfaces has any unpaired electron (Fig. 26b). These measurements confirm that the grown BN films are of high-quality and defect-free, and have a UWBG nonmagnetic nature.

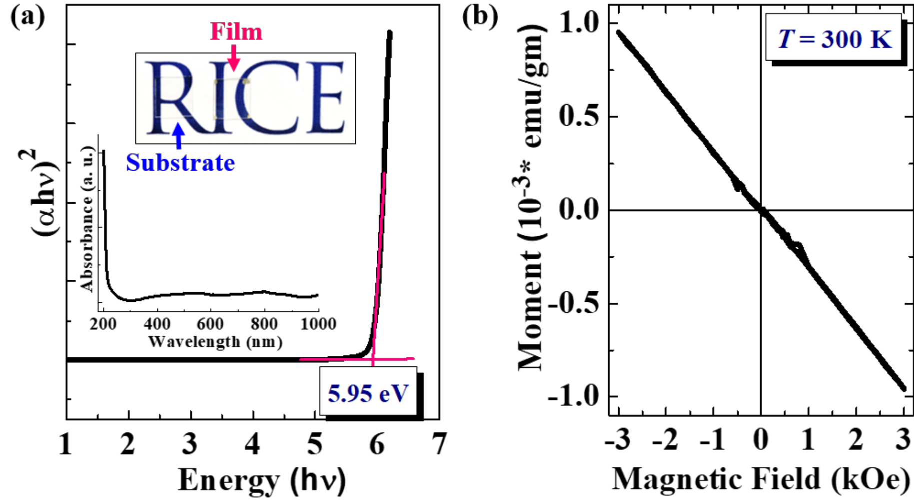

Fig. 26 Properties of BN–Al_2O_3 thin films. a) UV-visible absorbance and b) magnetization measurements showing the UWBG nature and nonmagnetic behavior. Inset shows the transparent nature of the film.

4.3.3.2 BN–GaN Thin Films

Wide-bandgap GaN is an important material for high-frequency semiconductor devices, along with other materials. Therefore, using GaN as a substrate to grow a UWBG BN film might be interesting for next-generation high-power, high-frequency devices. Therefore, we used GaN as a substrate to demonstrate the grown BN thin films.

We grew approximately 7-nm BN thin films on a GaN substrate using PLD at high temperature (800 °C) and 100-mTorr N_2 partial pressure. The GaN was grown by the metal organic CVD (MOCVD) method. As seen, the elemental XPS scan shows the formation of B–N peaks, with some residues of surface oxidation and contaminations related to the BN peaks (Fig. 27a and b). Moreover, FTIR and Raman show broad peaks, indicating the disordered growth of BN on GaN. AFM shows the surface morphology with a roughness of approximately 0.22 nm (Fig. 27c and d).

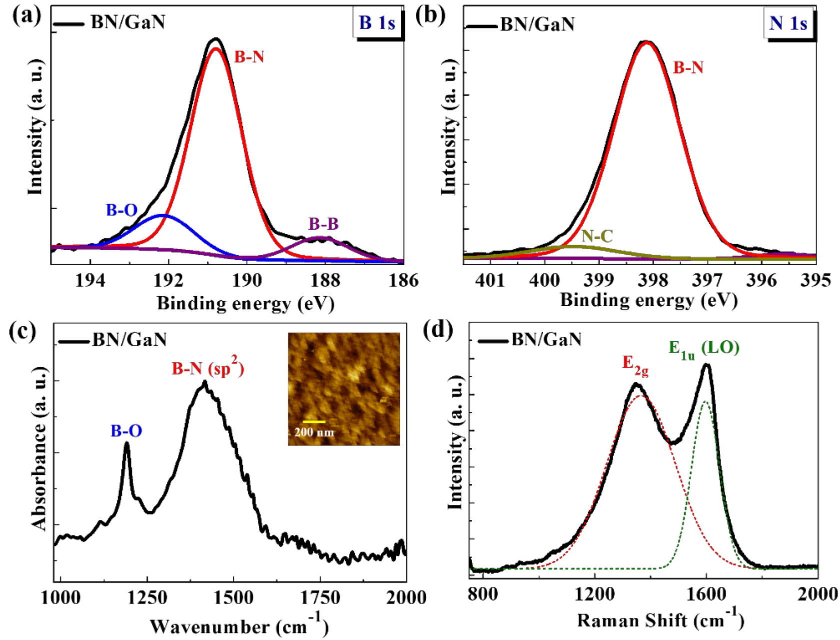

Fig. 27 Characterizations of BN–GaN films: a) elemental XPS scans, b) FTIR, and c) Raman spectra showing the growth of BN. Inset shows the AFM image of the film.

We also performed cross-sectional, high-resolution scanning transmission electron microscopy (STEM) of the BN–GaN film. As seen, grown GaN by MOCVD demonstrates a nice crystallinity and periodic ordering of atoms. We can also see a thin dense BN layer is sandwiched between the GaN and Au, however without any long-range ordering of the BN layers (Fig. 28), consistent with the structural characterization of defect-induced growth of BN. High-energy electron loss-spectroscopy (EELS) mapping also confirms the presence of BN layers.

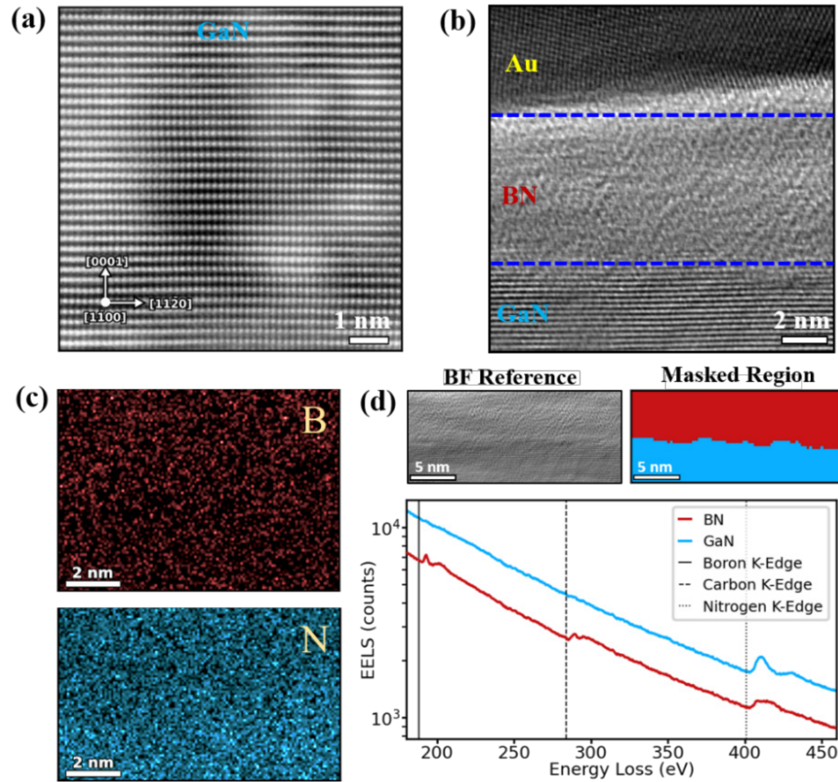

Fig. 28 Cross-sectional atomically resolved STEM images of the BN–GaN film. a) Grown GaN by MOCVD and b) BN layer grown by PLD. c) Energy dispersive X-ray (EDS) analysis mapping shows the uniform presence of B and N, and d) EELS mapping confirms the presence of B and N.

We also performed second-harmonic generation (SHG) of the BN–GaN film (Fig. 29), which shows that the grown BN film is SHG active. In general, from symmetry, for BN, the odd number layers are SHG active, whereas for even numbers, it dies out. However, several reports have also shown that thick BN, as well as defective BN films, is SHG active. From SHG, we obtained the second-order nonlinear susceptibility of 11.1 pm/V, which is in good agreement with the literature reports[18] and signifies that BN–GaN is also useful for optoelectronics.

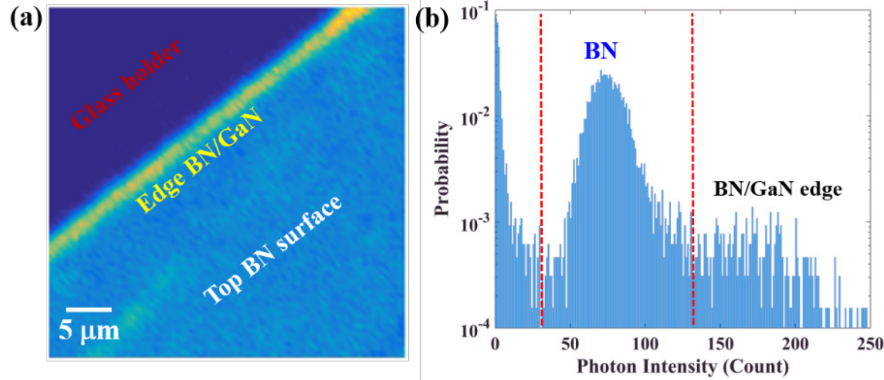

Fig. 29 Spatial SHG of BN–GaN film: a) intensity mapping and b) the probability vs. photon intensity count showing that the film is SHC active

4.3.3.3 BN–PCD Thin Films

As diamond is the most interesting substrate to achieve our goal, we first used PCD substrates to grow BN films. Commercially purchased PCD shows the major peak of (220). We have grown approximately 20-nm BN films at 800 °C and 100-mTorr N_2 pressure, both as-grown as well as in-situ post-annealing at the same growth temperature and pressure for 3 h. From XPS and elemental scans, we can see the presence of the characteristic B–N bonds, in both the B 1s core and N 1s core XPS, along with almost 1:1 elemental ratio (Fig. 30a). Interestingly, the surface morphology of the grown films shows distinct differences (Fig. 30b). In contrast to as-grown films, annealed films show much larger island sizes, again signifying the fact the in-situ high-temperature annealing improves the crystallite quality of the films. The surface roughness also reduced from 4.04 to 3.67 nm after the in-situ annealing.

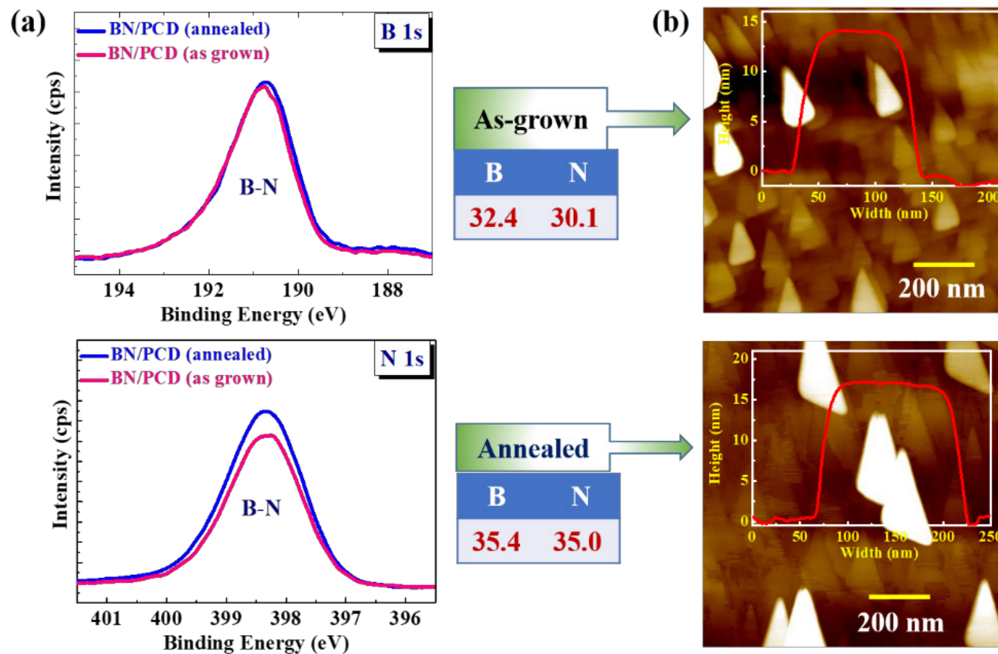

Fig. 30 Characterizations of BN–PCD films: a) XPS at B 1s and N 1s core of as-grown and in-situ 3-h annealed BN–PCD films and b) corresponding AFM surface topography

Furthermore, we have also grown BN films on in-house grown PCD using the Plassys CVD diamond growth reactor at Rice and compared it with the film grown on commercial PCD. As shown, from XPS, in both the cases, the features are very similar, suggesting that our home-grown PCDs are also of the same quality as commercial PCD (Fig. 31).

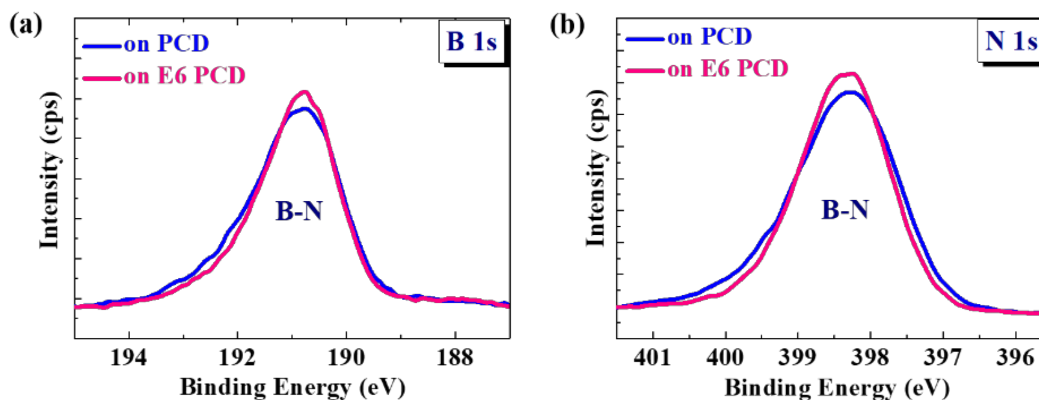

Fig. 31 Comparative XPS of BN–PCD films. Films were grown on a) homegrown PCD and b) commercially purchased PCD from Element Six.

4.3.3.4 BN–SCD Thin Films

Now we focus on BN growth on SCD substrates, using the same growth conditions as for PCD. After growing the films, we characterized them with XPS. As seen

from XPS, the films show B, N, and C 1s XPS peaks, and remarkably, the elemental ratio of B and N was exactly 1:1 (Fig. 32).

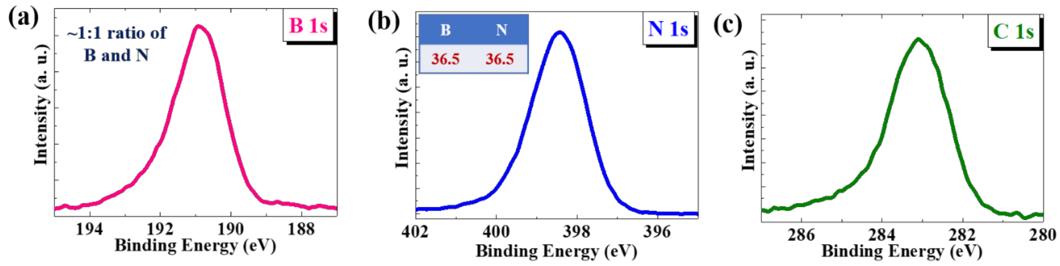

Fig. 32 XPS of BN film grown on normal-grade SCD: a) B 1s, b) N 1s, and c) C 1s cores

We further characterized using an XRD azimuthal scan, which shows fourfold symmetry of both diamond and BN, suggesting that it is most likely of a cubic nature (Fig. 33). The surface topography does show the 3-D island-like morphology; however, Raman spectra show the profound diamond peak, with the possible suppression of the c-BN Raman peak.

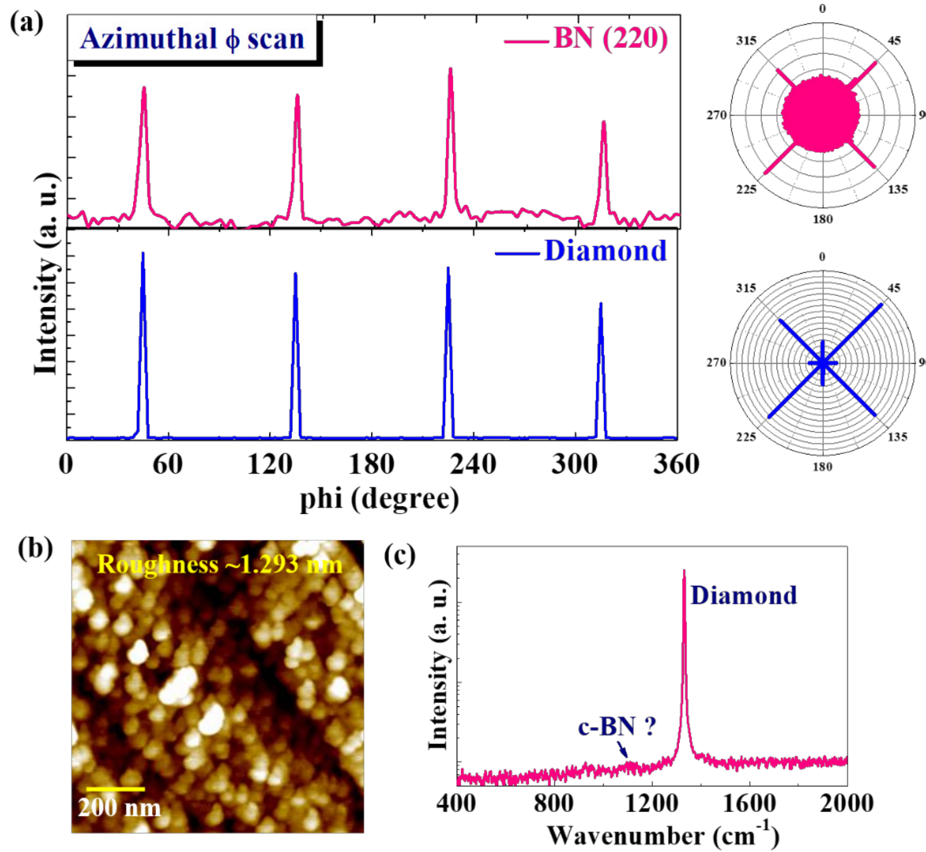

Fig. 33 Characterizations of BN–SCD films: a) XRD azimuthal symmetry phi-scan, b) AFM surface topography, and c) Raman spectra of a BN–SCD film

Then we performed the cross-sectional high-resolution TEM (HRTEM) of as-grown BN–SCD and in-situ annealed BN–SCD films. We can clearly see the formation of a dense BN layer, however, without any-long range atomic ordering (Fig. 34), suggesting that the grown BN films on SCD are of a disordered or nanocrystalline nature. We are currently working on more optimization of the BN–SCD films to obtain epitaxial c-BN–SCD thin films.

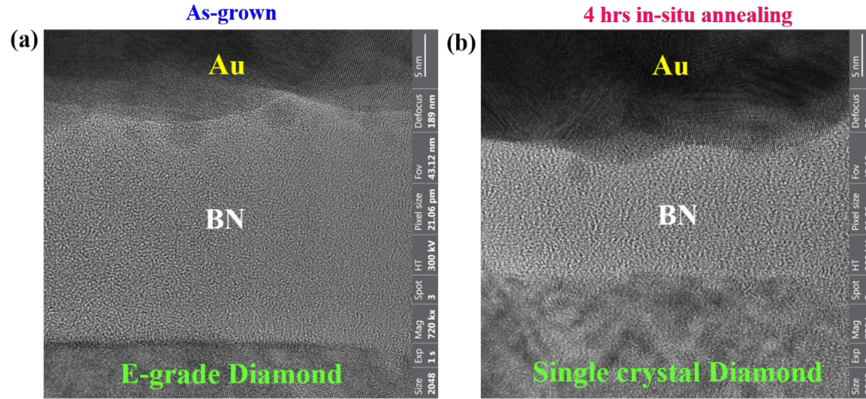

Fig. 34 Cross-sectional HRTEM images of BN–SCD films. a) As-grown and b) in-situ 4-h annealed film at the same growth temperature and pressure, showing the formation of a dense BN layer in between of diamond and Au.

5. State-of-the-Art Metrology Approaches Development of Characterization Techniques for Diamond–BN and Diamond–FET Interfaces

5.1 FIB Milling: Preparation of TEM Specimen from Bulk Structures

A FIB instrument appears and operates much like an SEM instrument. Both tools rely on a focused beam to create a specimen image, an ion beam for FIB and an electron beam for SEM. For both instruments, the flux of the secondary electrons created at each raster position of the beam is visualized to create an image of the sample. In FIB, secondary ions may also be detected and used to construct an image of the sample. Images with magnifications up to approximately 100,000× are available using a FIB with a very good depth of field. Though the microelectronics industry continues to push advancements in FIB instrumentation, FIB, however, is being evolved as a general characterization and sample preparation instrument for both the physical and biological sciences. The micron to nanometer beam size and imaging capabilities of FIB makes this instrument ideal for preparing site-specific SEM or TEM specimens in either cross-sectional or plan view. The beam can be very accurately focused on the sample at a high current density to produce large (i.e., 15 × 5 µm) but very thin TEM specimens (e.g., <100 nm) that can be prepared

in just a couple of hours depends on the sample density. The various steps involved in the process of "FIB lift-out TEM" specimen preparation from bulk samples (e.g., diamond–FET and diamond–BN heterostructures) are given and detailed in Fig. 35.

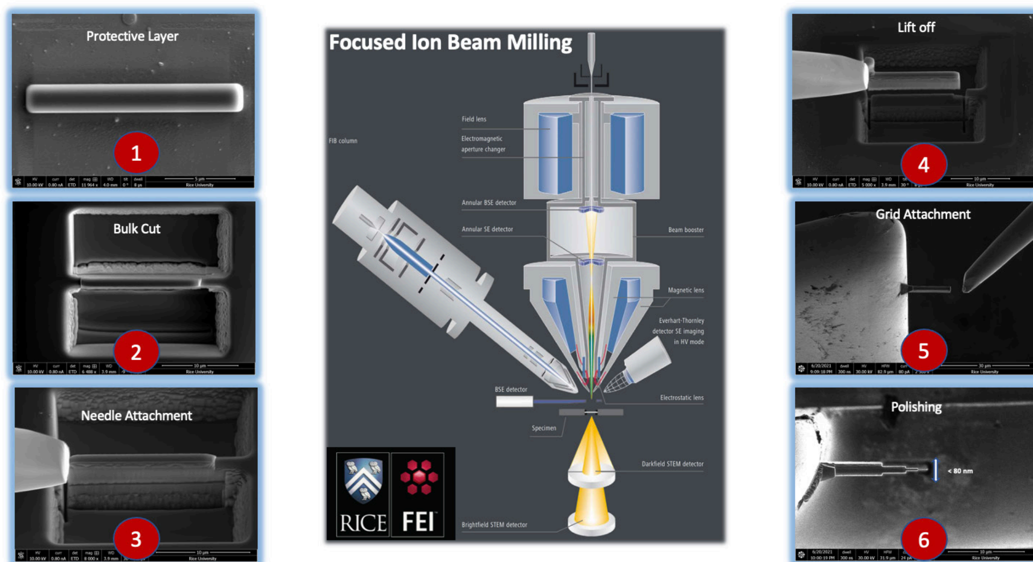

Fig. 35 Schematic of a FIB unit (middle) consisting of an electron beam, ion beam, metal and C gas source, and an easy needle for specimen movement (lift out). Step 1: Sputtering of a conductive protection layer. Step 2: Bulk cut followed by U cut. Step 3: Easy needle attachment. Step 4: Lift off the specimen from the surface. Step 5: Attachment of the specimen to the TEM half-grid post. Step 6: Polishing the specimen up to a thickness level of less than 100 nm.

The lift-out technique[19] requires little or no initial specimen preparation; the only requirement here is that the bulk sample must fit inside the FIB specimen chamber. Insulating materials are sometimes pre-coated with C, Au, platinum, or chromium to prevent charging. In a typical FIB process, the TEM specimen preparation starts with the deposition of a metal line using the electron beam first, followed by ion beam on the area of interest to prevent damage and spurious sputtering of the top portion of the specimen and also to delineate the location of the area of interest. Typical dimensions of the metal line are approximately 1.5 μm wide × 1.5 μm high × 15 μm long. Later, large trenches are sputtered on either side of the area of interest using a high gallium (Ga^{+}) beam current. Next, by properly tilting the stage, the bottom, left side, and a portion of the right side of the specimen are cut free before attaching the easy needle and cutting the rest of the right side off for lift-off. The specimen, approximately 1.5 μm wide × 5 μm high (including protection layer) ×15 μm long, is then attached to the Cu TEM grid post, followed by polishing to an electron transparency thickness range (approximately <100 nm). The lesser the thickness, the better the specimen will be under the electron microscope, which in turn helps to make high-resolution images. We are employing

a Helios Nano Lab 660 FIB unit to prepare the TEM specimens of grown diamond, diamond–BN heterostructures, and diamond-based FET devices.

5.2 Aberration-Corrected Electron Microscopy: Microstructure and Interfaces

TEM is maybe best known for forming images at the highest resolution. It has many other capabilities, of course, such as forming diffraction patterns, X-ray microanalysis (EDS), or EELS, to name a few, but the first item to be mentioned in an instrument's specification is probably its resolution limit. The various modes of this imaging and electron spectroscopy method are schematically presented in Fig. 36. In the last few decades, the performance of TEM has enhanced gradually but steadily, and the sample probing resolution has improved from 1 nm to 0.2 nm. Useful progress indeed, as most of the interatomic distances lie in the region of 0.2 nm. During the last few years, however, there has been a revolution in the attainable resolution limits with the arrival of aberration correctors for the objective lens. The improvement in the attainable resolution limits has been dramatic, described as a quantum leap. Correctors have been added not only to TEM but also to STEM. The obtainable resolution limit now lies at around 0.1 nm or better in both TEM and STEM, and the improved images from these aberration-corrected microscopes are opening new avenues in the characterization of materials.

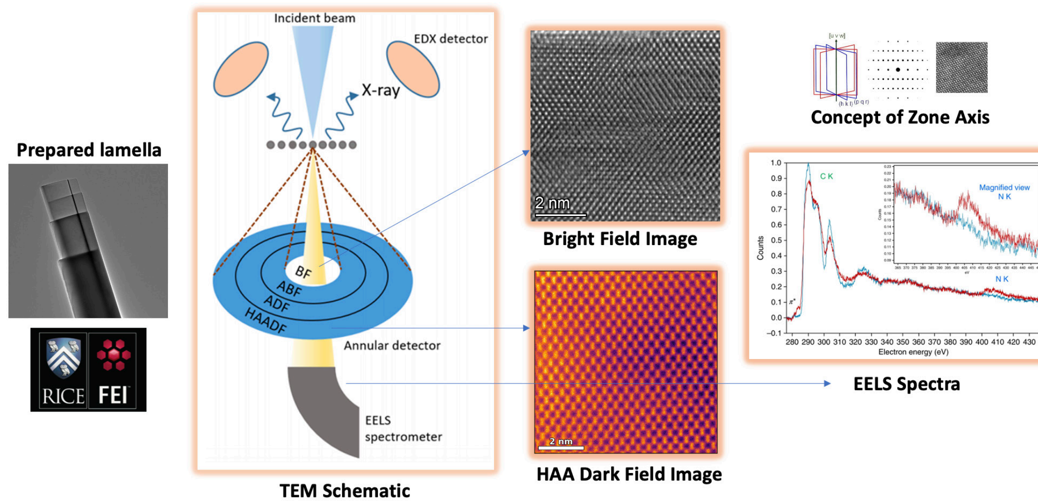

Fig. 36 **(Left) FIB-prepared TEM specimen; (middle) schematic showing the bright field, dark field, EDS, and EELS; and (right) corresponding microscopy images and EELS spectrum for CVD-grown SCD**

One of the basic limits to the resolution is defined by the wavelength, λ, of the electrons and the quality of the objective lens used to form the image. This limit is termed as the point resolution limit. However, mention must be made here of the other factors that limit resolution: 1) a virtual source size leads to limited spatial

coherence in the beam, 2) instrumental instabilities give the incident electron beam a range of wavelengths, and 3) chromatic aberration of the electron lens leads to incorrect focusing of the nonmonochromatic beam. These factors contribute to the so-called information limit.[20] The breakthrough came with the use of nonrounded lenses, the principle of which was first outlined by Scherzer in 1947. These multipole lenses can generate a negative value of Cs and thus can cancel the positive Cs of the round lens. There are two basic types of correctors: the quadrupole/octupole assembly and the hexapole assembly. Most of the TEMs now incorporate a scanning attachment in order to form STEM images. Here, the corrector used is hexapoles and can achieve the same result as the correctors based on the octupole/quadrupole design, a reduced probe size resulting in a higher-resolution STEM image, or an increased condenser aperture size that leads to better signal levels for microanalysis.

We are employing a Titan TEM (FEI Titan Themis3) at an acceleration voltage of 300 kV for performing electron microscopy. The unit is capable of performing TEM, STEM, EDS, and EELS. The samples that are bulk and need TEM specimen preparation (FIB) and microscopy analysis are the following and are schematically displayed in Fig. 37 and 38:

- Transfer-doped diamond FETs
- CVD-grown PCD and SCD wafers
- PLD-deposited diamond–BN heterointerfaces
- B-implanted diamond wafers

The diamond FET device TEM specimen preparation and TEM characterization follow, and the rest of the material's characterization is included with their respective growth discussion sections as appropriate.

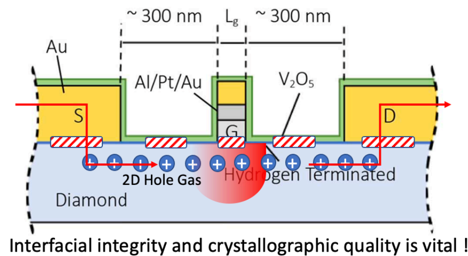

Fig. 37 Schematic of transfer-doped diamond FET, where the crystallographic quality of source and drain diamond channel interface need to be crystallographically intact and free from impurities and defects. Similarly, the gate dielectric and channel interface must ensure homogenous distribution of the transfer dopant as well (here it uses V_2O_5). Various interfaces of interest are flagged by red-patterned boxes.

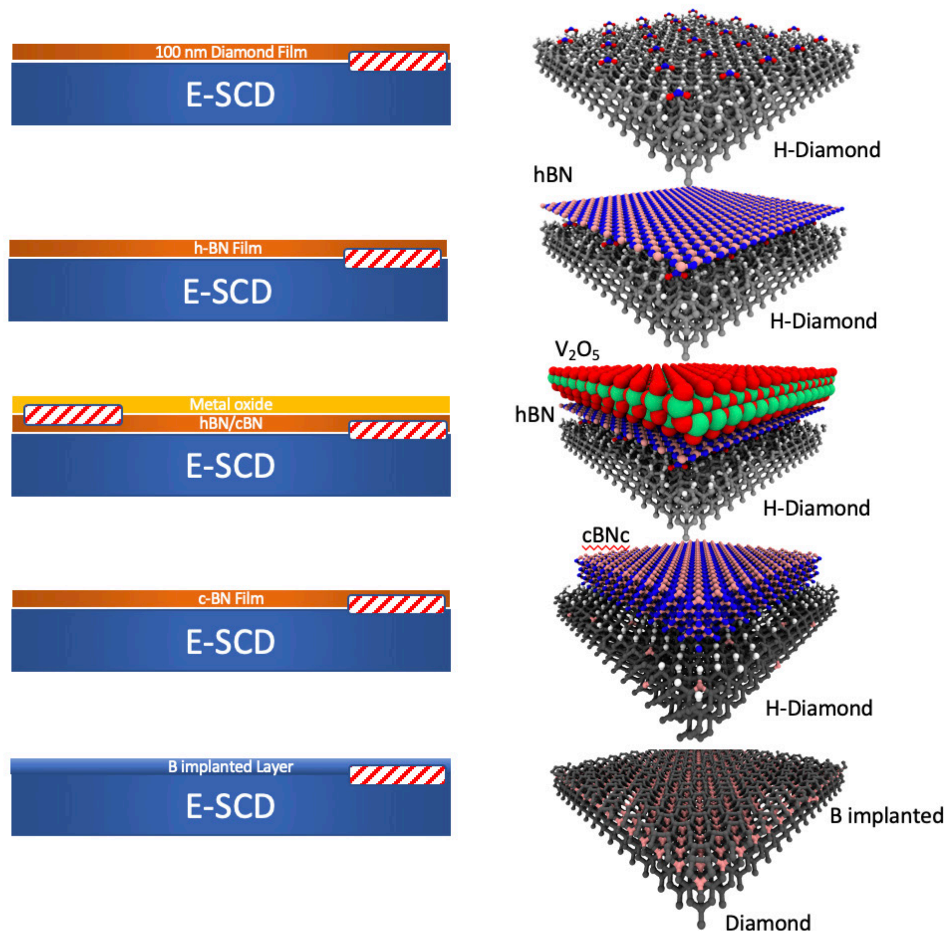

Fig. 38 (Top to bottom) The 100-nm thin layer of diamond grown on SCD wafer, PLD-deposited h-BN layer on electronic-grade SCD wafer, metal oxide–h-BN–SCD structures, PLD-deposited c-BN on electronic-grade diamond, and finally, the B ion–implanted single crystalline wafers. Various interfaces of interest are flagged by red-patterned boxes.

5.3 Diamond-Based FET (E46) Characterization

DEVCOM ARL has been working on the transfer-doped, diamond-based FET for a while and the E46 wafer FET devices are the best so far.[21] It is vital to correlate the structure, property, and device performances to understand the complete picture why one device is better than the other and so on, for which microscopy analysis is quite helpful. The layout of the E46 chip consists of several transistors; the pad layout is displayed in Fig. 39. To analyze the whole device, one needs to look at multiple transistors of different gate lengths and the pads at the periphery as samples. For E46, the regions and transistors of interests are E46-O-3, E46-P-9, E46, E46-I-11, and the test structure TLM #6. The top and cross-sectional views of the transistor are displayed in Fig. 35 (right) and of the TLM test structure in Fig. 35 (left). The TEM specimen of the transistors and pad were prepared by FIB milling and transferred to the TEM Cu half-grid stems. Unlike the conventional

conducting wafers such as doped Si, milling-insulating yet highly dense diamond wafers are not straightforward. The insulting nature may drift the sample during the milling procedure and may sputter even the area of interest under the protective layer. Milling the specimen under low accelerating voltage and current is the only way to circumvent this scenario, in turn dramatically increasing the milling time. For instance, if a conducting Si wafer takes 3 h to prepare the lamella, it may take up to 4–5 h to prepare a lamella of a diamond wafer sample.

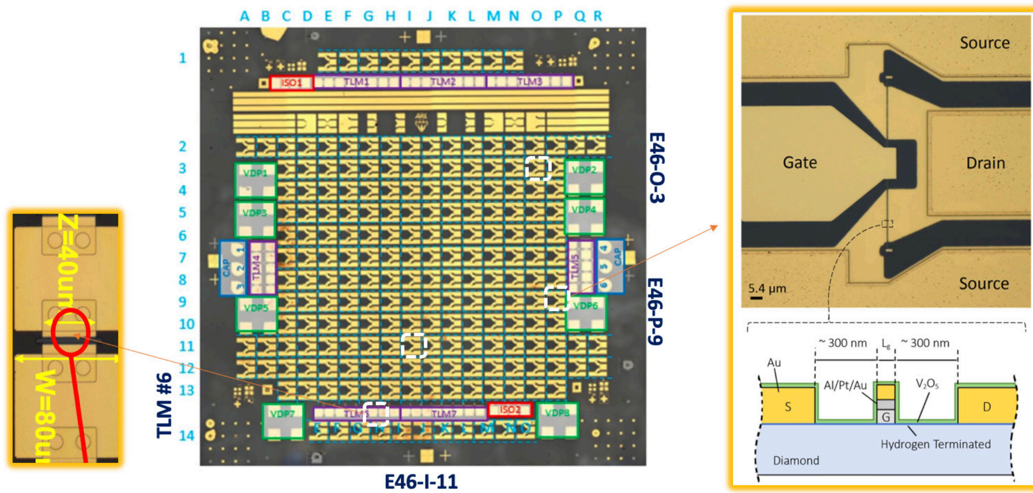

Fig. 39 Image of the E46 wafer with transistors of interest and pads flagged with the dotted rounded box (middle). (left) Top view of the pad (TLM #6) and (right) top and cross-sectional views of the transistor (E46-P-9).

A bird's eye view of various regions of interest of a transistor under a microscope is displayed in the Fig. 40, where regions from the source channel up to the drain channel are probed and displayed. Here the SCD area is used to align the lamella to the zone axis [110] and the STEM image presented is hence the (100) projection of the diamond crystal. One can see that all the interfaces are intact except a bubble-like void in the middle of the gate electrode. The metal oxide layer is also showing some degradation and manifesting some discontinues as patches across the channel region. Each of these regions is analyzed in detail and comprehended in Figs. 41–43 with the appropriate images and inferences.

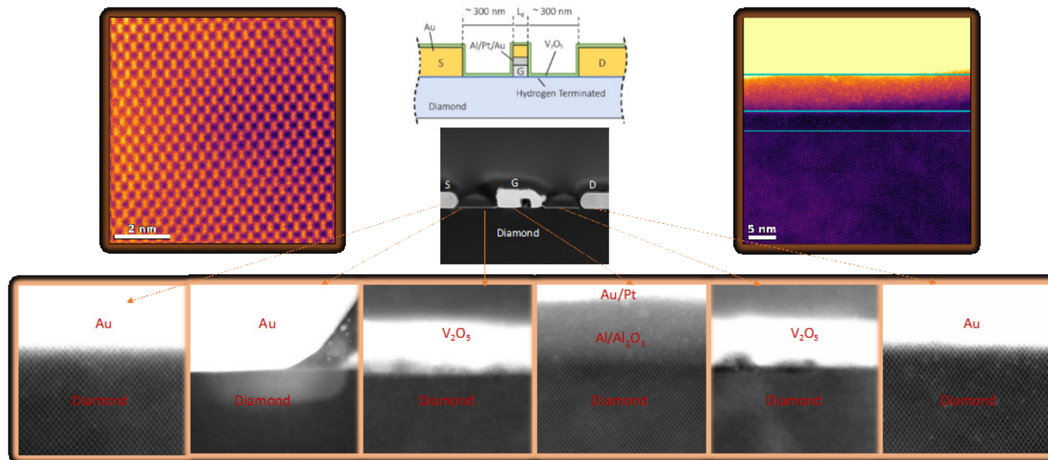

Fig. 40 (Left) (100) surface of electronic-grade SCD. (middle) Cross-sectional schematic image of diamond transistor and corresponding low-magnification STEM image. (Right) Channel-gate dielectric-gate electrode interface. (Bottom) Moderately magnified images: (from left to right) source–channel interface, source–diamond–channel interface, transfer dopant–channel–diamond interface, diamond–gate dielectric–gate electrode interface, diamond–channel–transfer dopant interface, and source–channel diamond interface.

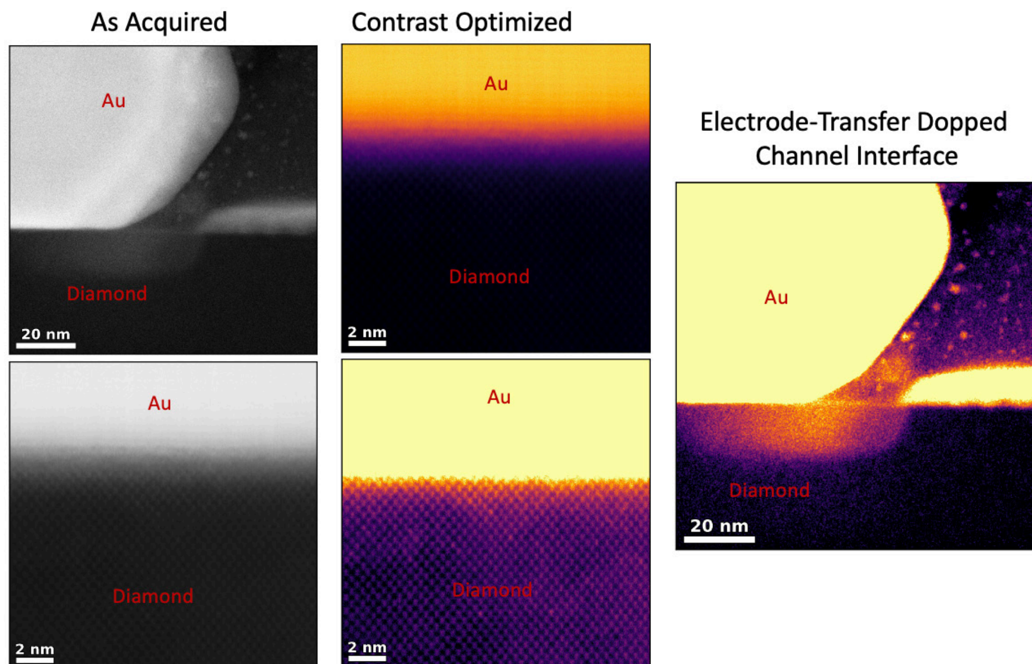

Fig. 41 Inference: the source contact–diamond interface is atomically sharp and crystallographically intact and free from any defects

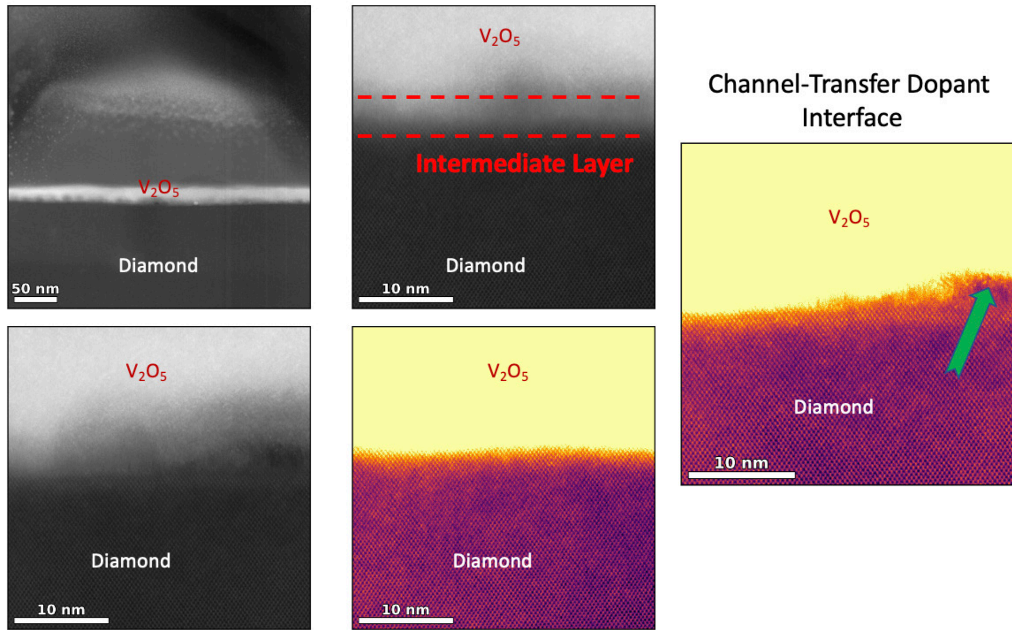

Fig. 42 **Inference: the metal oxide V_2O_5–diamond interface is 99% homogenous with some metal oxide deterioration due to the exposure of lamella to atmospheric moisture during the transfer from the FIB chamber to the TEM CompuStage**

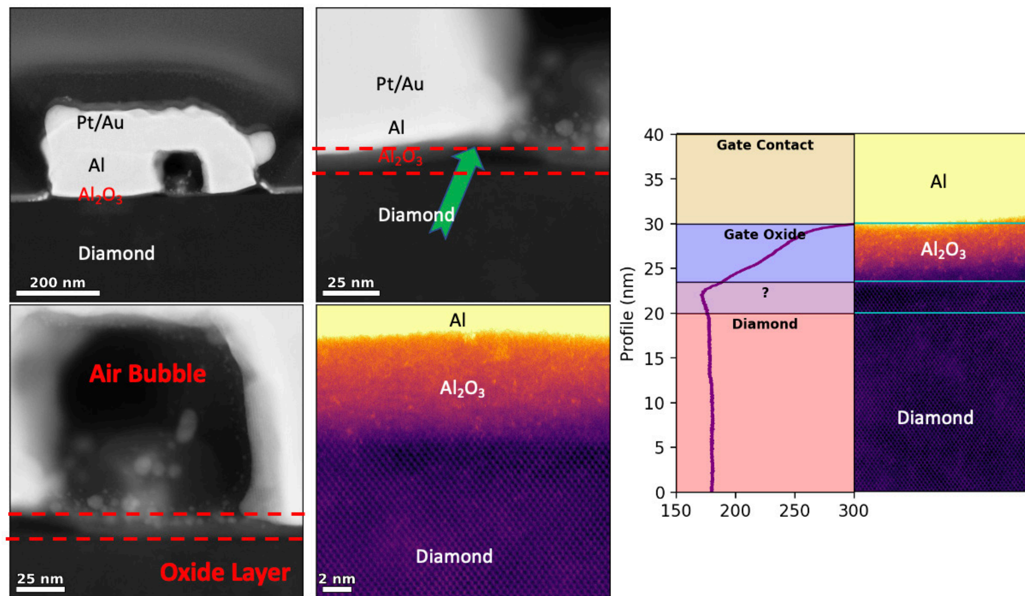

Fig. 43 **Inference: as expected, an amorphous metal oxide layer, Al_2O_3, is present between the gate–channel interface and a bubble-like vacuum area produced by the presence of trapped air bubble during the fabrication process and can also be seen in the high-magnification image**

5.4 Other Metrology Approaches

5.4.1 THz Spectroscopy: Electrical and Electronic Properties of H-Terminated Diamond

The advantages of ultrafast terahertz (THz) spectroscopy lie in its ability to yield the complex-valued, THz frequency-resolved conductivity spectrum of materials under study as a result of the interaction between the material and ultrashort subpicosecond single-cycle pulses of electromagnetic radiation with its frequency spectrum in the THz range. Conveniently, THz frequencies coincide with the typical electron/hole (carriers) momentum scattering rates in metals and semiconductors. Further, owing to the small photon energy (1 THz ≡ 4.1 meV), THz spectroscopy probes only the conduction of cold, Fermi-level electrons, in contrast to laser-excitation methods such as two-photon photoemission and SHG. Finally, THz spectroscopy is an all-optical method, and the absence of contacts in the measurements in addition to the (sub-) picosecond interaction timescale prevents any spin accumulation at the contacts. Most crucial, however, is the ability of THz spectroscopy to independently determine several carrier transport parameters at once. For example, in the case of Drude conductivity in metals and semiconductors,

$$\hat{\sigma}(\omega) = \frac{\sigma_{d.c.}}{1-i\omega\tau};\ \sigma_{d.c.} = \frac{e^2\tau N}{m^*}, \qquad (1)$$

where $\hat{\sigma}(\omega)$ is the AC conductivity, $\sigma_{d.c.}$ the DC conductivity, $\omega/2\pi$ the THz frequency, N the carrier density, τ the momentum scattering time, and m^* the effective mass.[22] We have been working on realizing the optical readout of the electrical properties of transfer-doped diamond wafers via THz–time-domain spectroscopy (TDS) and have progressed steadily during the past year. The samples under study are H-terminated PCD and SCD wafers and B-doped PCD wafers. The samples were kept under a moisture-free atmosphere to avoid the parasitic absorption of the THz probe beam by moisture during the measurements. The other side of this isolation is the charge-carrier density may be reduced as the surface adsorbent molecules will reduced under humidity-free conditions, hence the DC conductivity. The DC real and complex conductivity of the above-mentioned samples were probed and displayed in the Fig. 44. To ensure the accuracy, the derived conductivity values were matched with the values obtained via the conventional van der Pauw probe measurements. The values obtained were comparable; however, to benchmark the methodology, experiments are going on with metal oxide–deposited, H-terminated diamond wafers to ensure more or less the same carrier density throughout the samples during the measurement. The instrumentation used for the THZ-TDS measurement follows. A laser output of 775-nm wavelength with a 150-fs pulse duration and 1-kHz repetition rate is used

to pump a nonlinear crystal such as lithium niobate ($LiNbO_3$) and zinc telluride (ZnTe). $LiNbO_3$ generates a 0.3–1.6 THz broadband pulse, while ZnTe generates 0.3–2.5 THz. Detection of THz is achieved via electro-optic sampling using ZnTe.

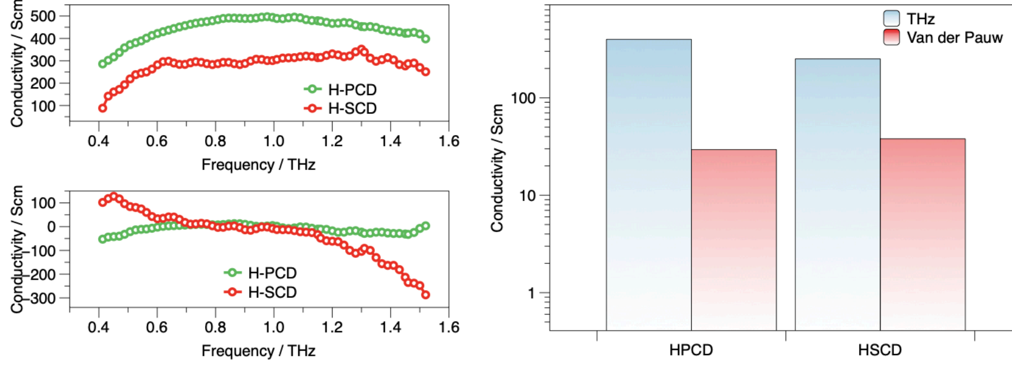

Fig. 44 (left) Real (top) and imaginary (bottom) conductivity values of H-polycrystalline and single crystalline wafers calculated through THs-TDS measurements. (right) Comparison between conductivity values measured using THz and conventional van der Pauw probe measurement. Conductivity values computed are comparable.

5.4.2 Cyclotron Resonance Measurements: Carrier Effective Mass Calculations

Cyclotron resonance (CR) is a method for determining the effective masses of charge carriers in solids. It is by far the most accurate and direct method for offering such information. In the simplest description, the principle of the method can be stated as follows. A particle of effective mass, m, and charge, e, in a DC magnetic field, B, executes a helical motion around B with the cyclotron frequency

$$\omega_c = \frac{eB}{m*}. \tag{2}$$

If an AC electric field of frequency, $\omega = \omega_c$, is applied to the system simultaneously, perpendicular to B, the particle will resonantly absorb energy from the AC field. Since B and/or ω can be continuously swept through the resonance and known to a very high degree of accuracy, m can be directly determined with high accuracy by $m* = eB/\omega$.[23] However, if the frequency of carrier scattering events (or the density of scatterers) increases, the CR linewidth increases, and, eventually, CR becomes unobservable when scattering (scattering time τ) occurs too frequently. To be precise, in order to observe CR, τ must be long enough to allow the electron to travel at least $1/2\pi$ of a revolution between two scattering events, that is,

$$\tau > \frac{T_c}{2\pi} = \frac{1}{\omega_c} \tag{3}$$

or

$$\omega_c \tau = \frac{eB}{m^*}\tau = \frac{e\tau}{m^*} = \mu B > 1, \quad (4)$$

where T_c is the period of cyclotron motion and $m\ \mu = e\tau/m^*$ is the DC mobility of the electron. In a realistic scenario, a free charge carrier with an effective mass of $m^* = 0.1\ m_0$ under an applied magnetic field (B) = 1 T will have a CR frequency of approximately $2 \times 10^{12}\ S^{-1}$; hence, one would need a microwave field with a frequency of 300 GHz to probe the resonance. However, to satisfy Eq. 4, one would need a material with a minimum mobility of $\mu = 1 \times 10^4\ cm^2/(Vs)$. Such a value of mobility can be achieved only in a limited number of high-purity semiconductors at low temperatures, thereby posing a severe limit on the observations of microwave CR. From the resonance condition $\omega = \omega_c$c, it is obvious that if a higher magnetic field is available one can use a higher frequency (or a shorter wavelength), which should make Eq. 4 easier to satisfy. Thus, all modern CR methods almost invariably use far-IR (FIR) (or THz) radiation instead of microwaves. Strong magnetic fields are available either in pulsed form (up to 10^3 T) or in steady form by superconducting magnets (up to 20 T), water-cooled magnets (up to 30 T), or hybrid magnets (up to 45 T). In our experimental setup, we can apply a magnetic field as high as 10 T and the CR probing frequency is in the THz range (0.25–2 THz). The curves obtained for an H-terminated electronic-grade single-crystalline wafer at different applied magnetic fields are appended in Fig. 45.

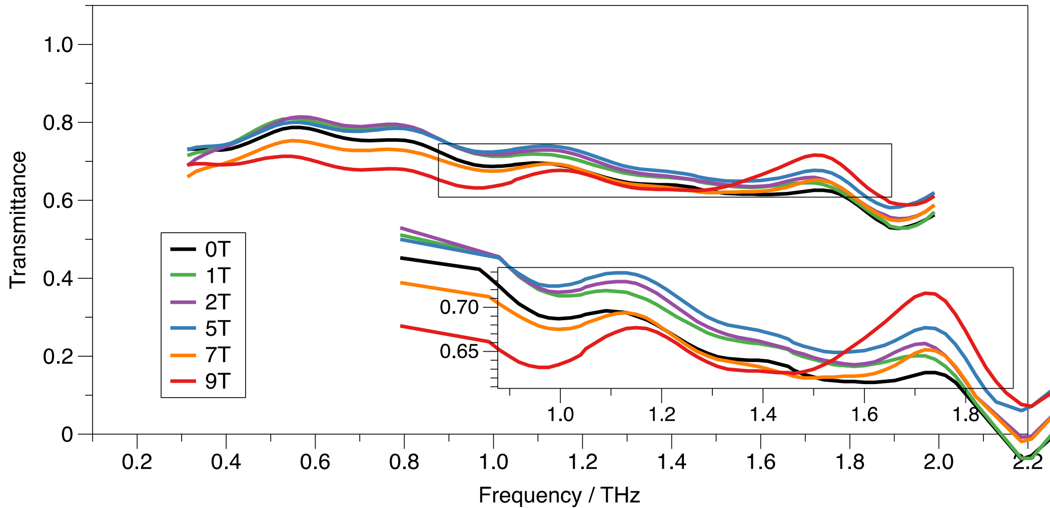

Fig. 45 The CR signal from an H-terminated SCD wafer is very feeble and found to have no change in the frequency range with respect to the applied magnetic field. This implies either the mobility of free carriers is too low, or under vacuum or humidity-free conditions, the carrier density is too low due to the lack of atmospheric transfer doping species.

Even after applying the highest magnetic field available, we observed a very feeble CR response from the H-terminated diamond wafers. This could either be due to

very low mobility of the 2D hole gas on the diamond surface or could be due to very low density of the free carriers. As the H-terminated wafers were kept under vacuum, which is a moisture-free environment, the transfer dopants such as water (H_2O), nitrogen dioxide (NO_2), and so on may be unavailable, hence the poor doping and carrier density. Presently, we are performing an experiment with transition metal oxide (TMO)-coated SCD and PCD wafers, which could possibly alleviate the latter issue discussed, but an improved mobility is still desirable to obtain a strong CR from the free carrier from the diamond surface.

5.4.3 Ellipsometry: Film Thickness, Roughness, and Optical Constants

Ellipsometry determines the change in polarization of polarized light as it reflects or transmits from a material. The polarization change is denoted as the phase difference, Δ, and the amplitude ratio, Ψ. The measured response is contingent on the optical properties and thickness of materials of interest. Hence, ellipsometry is generally used to determine optical constants and film thicknesses. However, ellipsometry is also used to characterize the roughness, doping concentration, composition, crystallinity, and other material properties that influence the optical response. Today, the range of its applications has spread to the semiconductor and data storage solutions, basic research in physical sciences, flat panel display, communication, optical coating industries, and biosensors. This widespread use can be justified by the increased dependence on thin films in many areas and the versatility of ellipsometry to measure most material types: dielectrics, semiconductors, metals, superconductors, organics, biological coatings, and composites of materials.[24]

Two parameters are used to describe the optical properties of materials that identify quantitatively how light interacts with a material. They are represented as a complex number and a complex refractive index ($\tilde{n}$) consisting of the index (n) and extinction coefficient (k):

$$\tilde{n} = n + ik. \tag{5}$$

Otherwise, the optical properties can be represented as the complex dielectric function:

$$\tilde{\varepsilon} = \varepsilon + i\varepsilon_2 \text{ and are related by } \tilde{\varepsilon} = \tilde{n}^2. \tag{6}$$

Finally, light loses intensity in an absorbing material according to Beer's Law:

$$I = I_o\, e^{-i\alpha x}, \tag{7}$$

where α is the extinction coefficient. Thus, the extinction coefficient relates how quickly light vanishes in a material. The data analysis proceeds after the ellipsometry measurement, as described in the following section. The schematic

showing the various components of an ellipsometer and the flowchart for ellipsometry analysis are given in Fig. 46. After performing ellipsometry on a sample, a model is defined to describe the sample. This model calculates the predicted response from Fresnel's equations, which identify each material in terms of optical constants and thicknesses. If these values are not known, an approximate value is given for the purpose of the preliminary calculation through iterations. Later, the calculated parameter values are compared to experimental data and any unknown material properties can then be varied to find the ideal curve fitting, which in turn improves the match between experiment and calculation. As usual, the number of unknown properties should not exceed the amount of information contained in the experimental data.

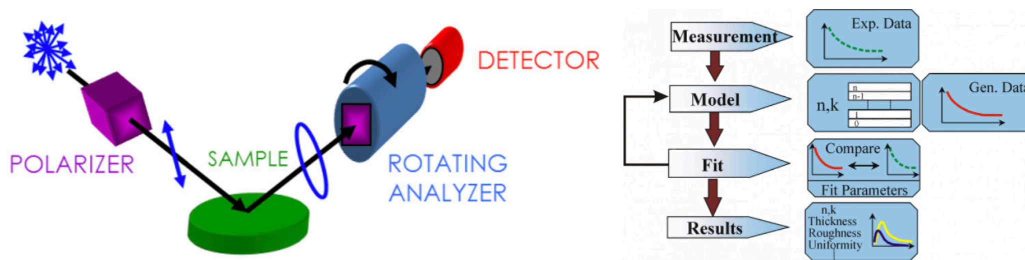

Fig. 46 (Left) Primary tools for collecting ellipsometry data: light source, polarization generator, sample, polarization analyzer, and detector. (Right) Flowchart showing the common procedure used to deduce material properties from ellipsometry measurements, which is basically a regression analysis as an exact equation describing the sample cannot be written. (Image courtesy of J.A. Woollam Ellipsometry Solutions.)

We have performed ellipsometry measurements on H- and O-terminated diamond wafers to study the change in refractive indices caused by such functional group terminations, and how the refractive indices (n) and extinction co-efficient varies in H- and O-terminated diamond is appended in Fig. 47. Since we have used the polished (either side) diamond wafers, the experimental curves are heavily interfered with the background reflection data, making the fitting part difficult. Experiments are going on with diamond wafers with slightly scratched/roughening bottom surfaces and we expect to get much-refined optical, dielectric, and depth thickness profiles of the functionalized surfaces.

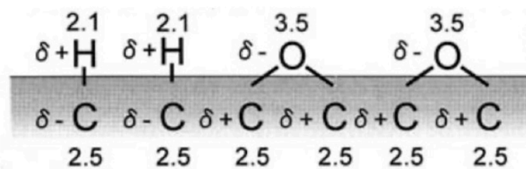

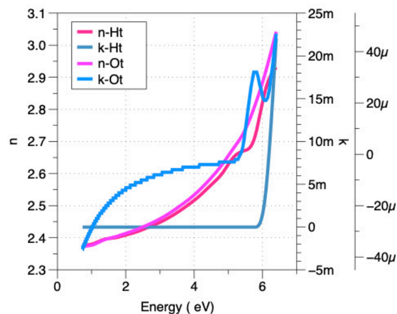

Fig. 47 (Left) Schematic illustration of the H- and O-terminated (100) diamond surfaces and (right) the formation of surface dipoles at H- and O-terminated diamond surfaces due to the difference in the electronegativity between C, H, and O.

6. Diamond Surface Modification and Doping: Amine, Amene, and Bromination of Diamond Surfaces

Due to its unique build blocking of sp^3 hybridization C, diamond is known as the material with the highest thermo-conductivity, mechanical hardness, and so on.[25] All those properties make diamond as an excellent candidate in many applications.[26] Hydrogenated diamond (HD), on the other hand, has attracted tremendous attention recently due to the negative electron affinity (NEA; –1.1 ~ –1.3 eV) effect observed on the surface.[27] As compared with bare diamond, the surface with additional hydrogen attachment will be electro-conductive on the order of 10 kΩ/ϒ when exposed to ambient air.[28] This can be ascribed to the enhancement of the carrier concentration (to 1×10^{13} cm^{-2}) on the surface.[29] Subsequently, the discovery was applied on device fabrication, such as a FET with a high RF output power (2.1 W/mm at 1 GHz) and high maximum frequency of oscillation (120 GHz).[30] Due to this success, effort has been dedicated to promoting the hole mobility and/or carrier concentration to further modify the sheet resistance of the diamond surface. Reports have shown that the exposing HD to 2% NO_2 enhances the hole sheet concentration up to 2.3×10^{14} cm^{-2}, which is 20 times higher than that of HD exposed to air.[31] However, after 93 h of NO_2 activation, the peak feature belonging to the NO_2 group drops severely, as observed in the FTIR spectrum, which suggests the instability of NO_2 attachment on HD.[32] As NO_2 is physically absorbed on the HD surface, the detachment will naturally occur once it is exposed to air with a low NO_2 concentration.

In this sense, a functional group that results in enhanced electronic properties while having a more stable attachment on HD surface is critical to ensure the sustainability and high performance of electronic devices. Enlightened from the previous experimental progress, the investigation of amination of diamond was carried out because of the proved NEA performance induced by the primary amine group (–NH_2) and its relatively stable attachment on the diamond surface.[33] In our

work, we developed a general procedure for diamond amination by UV irradiation in ammonia gas. The highest N concentration resultant from our route was 6.4% on the diamond surface, in which more than 90% of N-related groups were found to be $–NH_2$. Interestingly, the surface cleaning effect was observed after amination with the assistance of XPS and SEM. In these senses, we proposed that our research could end up with a facile-cleaned N-terminated diamond with an NEA effect, which is useful for electronic device fabrication.

The amination of diamond involved multiple steps. First, the hydrogenation of the diamond surfaces was conducted using the electrochemical method.[34] Two electrodes system were employed, where two pieces of B-doped diamond (BDD) were reacted as the anode and cathode, respectively. All the electrolytes were degassed before use. The target BDD film was first submerged in 100 ml of 0.2 M sulfuric acid (H_2SO_4) solution and oxidized under +100 mA for 5 min. After cleaning with distilled water, the film was immersed in a 500-ml solution of 2 M H_2SO_4 and reduced under –1.05 A for 40 min. Second, the partial oxidation of hydrogenated BBD (HBDD) was achieved by immersing HBDD in a H_2SO_4/HNO_3 mixture (9:1) and piranha solution (H_2SO_4/hydrogen peroxide [H_2O_2], 3:1), respectively. The reaction was carried out at designed temperatures (100, 190, and 290 °C) for 5 min, respectively. After the reaction, the solution was cooled down to room temperature naturally before it was diluted with distilled water. The partial oxidized HBDD (O-HBDD) samples were taken out using an acid-resistant tweezer and sonicated in distilled water for 20 s. Third, a piece of O-HBDD film, 10 ml of hydrogen bromide (HBr), and a stir bar were placed into a three-neck boiling flask to which an Allihn condenser was connected. Then, the system was heated up in an oil bath at designated temperatures (55, 80, and 105 °C) for 40 h, respectively. After the treatment, the solution was diluted with deionized water. The sample was picked up using an acid-resistant tweezer and sonicated in deionized water for 20 s. Fourth, HBr-O-HBDD was placed on a crucible and inserted into a quartz tube. The UV lamp (GPX 13, 13.4 W, 254 nm) was kept approximately 2.5 cm above the O-HBDD. The quartz tube was first purged with Ar for 20 min. Then, anhydrous ammonia was introduced and subsequently the Ar was switched off. The reaction was kept for 6 h under UV light irradiation. After ammonization, the BDD samples were stored in a vacuum desiccator before characterization.

As compared with pristine BDD in Fig. 48a, HBDD illustrates additional peak formations around 2800–3000 and 3200~3600 cm^{-1}, which are representative of C–H and C–OH groups, respectively. However, it can be seen that after HBDD is partially oxidized, the peaks of C–H groups diminish. HBDD oxidized by H_2SO_4/HNO_3 at a ratio of 9:1 under 190 °C (O190-HBDD-1) presents higher C–H and C=O peaks than that of HBDD oxidized by H_2SO_4/H_2O_2 at a ratio of 3:1 under 190 °C (O190-HBDD-2), indicating O190-HBDD-1 is left with a higher amount of

C–H and C=O groups after oxidation. Subsequently, the aminated 190-HBDD-1 is chosen to demonstrate the success of diamond amination. The new peak identified around 3200~3400 cm^{-1} can be ascribed to the formation of $–NH_2$ group, simultaneously; diminishment of the C–H group is also observed. This manifests as the C–H is converted to the amine group after the amination. In light of this progress, the optimization of amination procedure is further carried out by adjusting the heating temperature of the oxygenation methods and the subsequently HBr treatment. Note that we found HBr treatment to be crucial for further promoting the N concentration on the diamond surface.

In Fig. 48b, as compared with BDD and HBDD, O190-HBDD-1 and O190-HBDD-2, respectively, present the highest N concentrations among the applied temperatures (100, 190, and 280 °C), where O190-HBDD-1 shows the higher amount of N attachment after amination. This indicates that a 9:1 H_2SO_4/HNO_3 weight for the peroxidation of diamond and 190 °C can best promote the amination process. Furthermore, employing an HBr treatment was found to be beneficial as it enhances the facile N concentration, approximately 6.4%, on O190-HBDD-1 treated by HBr under 80 °C (Fig. 48c). However, the boosting effect is not observed on the O190-HBDD-2 samples. This might be correlated with a different reaction mechanism occurred between HBr and the O190-HBDD-2 surface.

We further analyze the XPS N 1s core spectrum to reveal the group information of aminated HBr80-O190-HBDD-1 and HBr55-O190-HBDD-2, as shown in Fig. 48d. Dominating coverage (more than 90%) of the NH_2 group is observed on aminated HBr80-O190-HBDD-1, whereas aminated HBr55-O190-HBDD-2 has only approximately 64% of NH_2 moiety among its N-related groups. With these interesting discoveries, the morphology of aminated BDD is further characterized by SEM (Fig. 48e and f). The sample after amination treatment shows a smoother surface in contrast to pristine BDD, implying a surface smoothening effect from the ammonia treatment.

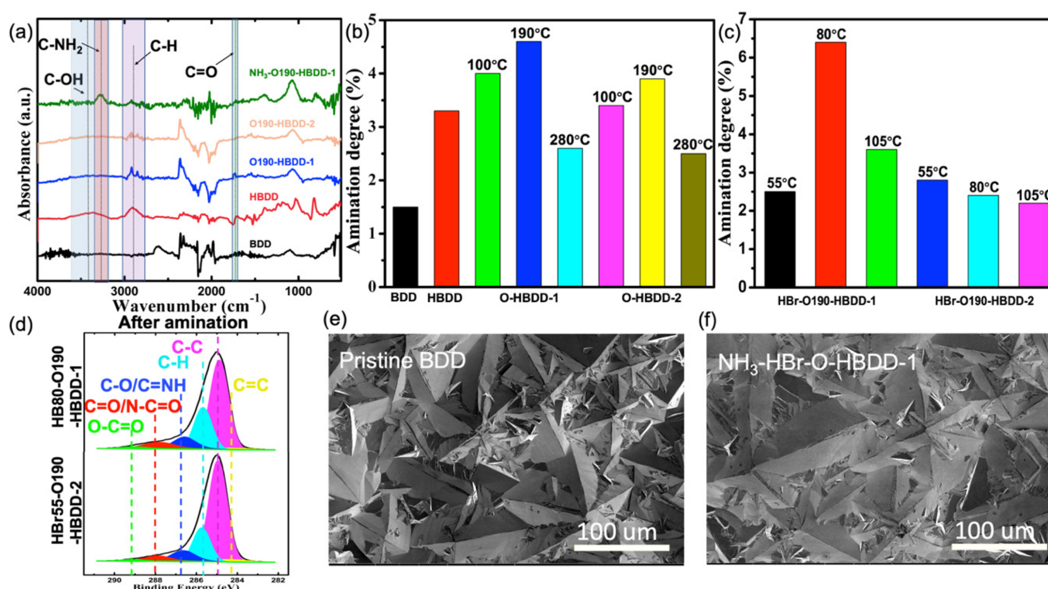

Fig. 48 Information on the functional groups resultant from different treatments as revealed by ATR–FTIR spectroscopy: a) N concentration of the samples b) with and c) without the HBr treatment, calculated from high-resolution XPS. The ratio of N-related groups d) in aminated samples, resolved from XPS N 1s core, and the morphology of e) pristine BDD and f) aminated BDD by SEM.

In the future, we plan to extend the scope to thiol and bromine terminations on the diamond surface to see how those moieties will influence the electronic properties of the resultant surfaces using computational modeling.

7. Theoretical Studies Performed with Classical and Quantum Theory Levels

7.1 Adhesion Energy Estimates of Diamond–BN Structures

When h-BN or c-BN is transferred to the diamond surface, it is important to evaluate how strong the interface formed is. As diamond can have different facets exposed at the surface, the different C atom arrangements also affect the interactions between h-BN or c-BN and diamond. One way to evaluate the strength of the interface is to estimate the adhesion energy, which is a measure of how strong the adhesion between the materials in contact is, or, in other words, the energy needed to undo the interface.

We performed a theoretical study to evaluate the adhesion energy between different diamond facets and BN (hexagonal and cubic). To do so, we employed reactive molecular dynamics (RMD) simulations using a reactive force field (ReaxFF). Our models consist of bare and hydrogenated diamond slabs of approximately 5×5 nm^2 (~5000 atoms), and on top of these slabs, we placed 1) one h-BN sheet of 4×4 nm^2

(~558 atoms) and 2) a c-BN (001) slab of 4.2 × 4.2 nm^2 (2300 atoms) with a thickness of 0.64 nm. In these simulations, we used different diamond facets to test the interaction with BN: (001), (110), (013), (111), and (113). In Fig. 49, we present some cases tested. All these systems were thermally equilibrated at 300 K for 1 ns on an NVT ensemble. A Nosé–Hover thermostat was employed to control the system temperature. The adhesion energy was estimated by Eq. 8:

$$E_{AE} = \left| \frac{(E_{S1} + E_{S2}) - E_{S1S2}}{A} \right|, \tag{8}$$

in which E_{AE} is adhesion energy (energy/area), E_{s1} the energy of slab 1, E_{s2} the energy of slab 2, E_{s1s2} the energy of the heterostructure, and A the area of the interface. With this definition, the higher the E_{AE}, the easier it is to form the interface. From the RMD simulations, we used the saturated total energy of the systems after the 1 ns of thermalization.

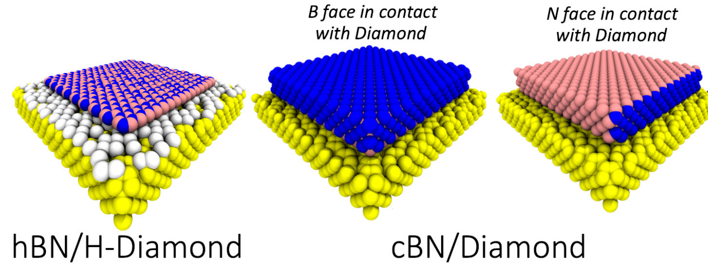

Fig. 49 Example of the models used to evaluate the adhesion energy, E_{AE}: an h-BN sheet on a hydrogenated diamond (001) face and c-BN on a bare diamond (001) face. For c-BN, there are two possibilities: c-BN face rich in either B or N atoms in contact with the diamond surface.

In Table 2, we present the averaged results from all cases studied. As can be seen, the highest E_{AE} is found for the h-BN on a bare diamond, and the lowest one is found for the c-BN on a hydrogenated diamond, when c-BN has a face with a higher concentration of B atoms. As h-BN is more flexible than c-BN, h-BN can buckle easily to accommodate to the diamond surface topology, which increases its adhesion.[35,36]

Table 2 Adhesion energy between h-BN and c-BN on bare and H-terminated diamond surfaces

Bare surface			**Hydrogenated surface**		
System	**<E_{AE}> (meV/Å^2)**	**<d> (Å)**	**System**	**<E_{AE}> (meV/Å^2)**	**<d> (Å)**
h-BN–D	47.87	2.48	**h-BN–HD**	15.13	2.78
c-BN–D – type 1[a]	15.67	2.50	**c-BN–HD – type 1[a]**	3.99	2.56
c-BN–D – type 2[b]	11.03	2.67	**c-BN–HD – type 2[b]**	17.91	2.51

[a] c-BN has a B face in contact with bare and hydrogenated diamond surfaces.
[b] c-BN has a N face in contact with bare and hydrogenated diamond surfaces.

7.2 Interfacial Energy Estimates for c-BN Grown on Diamond Surfaces

We also tested theoretically the feasibility of c-BN to be grown directly on diamond surfaces. To do so, we evaluate the interfacial energy (E_{int}), which represents the cost to create/form an interface between two materials. E_{int} can be estimated theoretically by Eq. 9:

$$E_{int} = (\gamma_1 + \gamma_2) - E_{AE}, \tag{9}$$

where E_{AE} is the adhesion energy (energy/area), γ_1 the superficial energy of slab 1, γ_2 the superficial energy of slab 2, and E_{int} the interfacial energy. We can see that the possibility to form an interface is described by a balance between the energy to form the surface (γ) and the energy under which they remain attached (E_{AE}). So, the lower the E_{int}, the higher the probability to form an interface.

Using density functional theory (DFT), we explore the E_{int} of several c-BN–diamond interfaces: 1) c-BN (001)–D(001)1×1 and c-BN (001)–D(001)2×1 (two types of c-BN contact to diamond, B or N face; lattice mismatch of 3.044%); 2) c-BN (110)–D(110) (lattice mismatch of 3.059%); and 3) c-BN (111)–D(111) (two types of c-BN contact to diamond, B or N face; lattice mismatch of 3.041%). These systems are presented in Fig. 50. Before estimating the E_{int}, we calculated the superficial energy of the isolated slabs. All simulations were performed with DFT using a projector augmented wave potential in a generalized gradient approximation using the Perdew, Burke, and Ernzerhof exchange-correlation functional. For the geometry optimizations, a Monkhorst–Pack k-mesh of 6 × 6 × 1 was used to sample the Brillouin zone and the Kohn−Sham orbitals were expanded in a plane-wave basis set with a kinetic energy cutoff of 50 Ry (~ 680 eV).

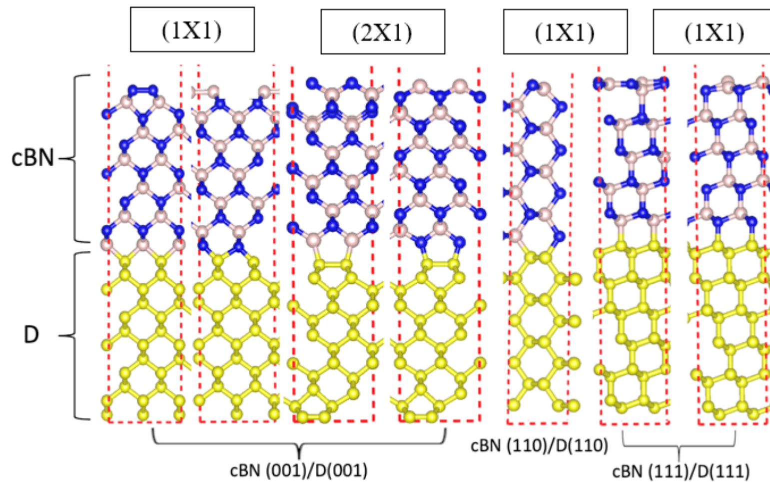

Fig. 50 h-BN–diamond and c-BN–diamond heterostructures used to estimate the interfacial energy, E_{int}

The results obtained for the interfacial bond length, E_{AE}, and E_{int}, are presented in Table 3. As can be seen, the highest E_{AE} is found for the c-BN (001)–D(001)1×1 with B atoms bonded to C ones. However, the lowest E_{int} is found for the c-BN (111)–D(111) with B atoms bonded to C ones. These results suggest that the interface that has the highest E_{AE} is not necessarily the easier one to form due to the cost to create a surface of c-BN on diamond (superficial energy γ). Then, according to the balance between the superficial energy of c-BN and diamond, and the adhesion energy between them, our results suggest it is easier to grow c-BN (111) on diamond (111). In summary, c-BN (111)–D(111) with B atoms bonded to C ones presents the lowest E_{int}, and hence, indicates a B-rich environment to the preferred condition for c-BN (111) growth on a diamond (111) surface.

Table 3 Theoretical interfacial bond length, E_{AE}, and E_{int} for c-BN–diamond heterostructures

Heterostructure	Interfacial bond length (Å)	E_{AE} (eV/Å^2)	E_{int} (eV/Å^2)
c-BN-001–D-001 1×1 (B)	1.67 (C-B)	0.897	0.168
c-BN-001–D-001 1×1 (N)	1.38–1.64 (C-N)	0.735	0.252
c-BN-001–D-001 2×1 (B)	1.59 (C-B)	0.666	0.179
c-BN-001–D-001 2×1 (N)	1.42 (C-N)	0.724	0.137
c-BN-110–D-110	1.61 (C-B)–1.52 (C-N)	0.622	0.079
c-BN-111–D-111 (B)	1.65 (C-B)	0.673	0.015
c-BN-111–D-111 (N)	1.53 (C-N)	0.515	0.141
Average	. . .	0.690	0.139

8. Collaborations between the Rice Team and DEVCOM ARL Team

The Rice team and DEVCOM ARL team have been working closely since the project started. In addition to having biweekly meetings, both teams have had a lot of interactions, discussions, and specimen exchanging. Table 4 lists some of the samples exchanged between the Rice team and DEVCOM ARL team.

Table 4 Samples exchanging between Rice and DEVCOM ARL

Exchanged samples	No. of samples	Purposes	Rice→ DEVCOM ARL	DEVCOM ARL→ Rice
Pristine PCD, SCD, ESCD	>13	Surface hydrogenation	Y	Y
Hydrogenated ESCD	3	Annealing and h-BN direct growth	Y	Y
h-BN transferred on diamond	4	Hydrogenation and electrical measurement	Y	Y
Boron implanted SCD, ESCD	5	N-type doping diamond	Y	
Diamond device wafers	2	Observing cross-section interfaces by FIB and TEM		Y
Oxidized diamond powder and PCD	>6	Characterizations	Y	
Patterned diamond devices	…	h-BN transfer		Y

9. Conclusions

This report assembles various research activities as part of the Cooperative Agreement (CA) between Rice and DEVCOM ARL. These efforts focus on the joint collaborative work between the two institutions in developing diamond as the next-generation UWBG material for electronic devices. The Rice team has excellent experience in the growth and development of high-quality materials and the DEVCOM ARL team has outstanding experience in developing diamond-based devices. The synergies were developed during the first year of the project and a strong collaborative team has been formed.

With the help of DEVCOM ARL and significant investment from Rice, a state-of-the-art diamond growth facility has been created at the newly formed center at Rice. The facilities to grow high-quality diamond are now ready and the third year of the program will see rapid progress in the preparation of high-quality samples that will be used by the DEVCOM ARL team to build devices. Growth of SCD substrates as well as heteroepitaxial growth of diamond and c-BN will be a significant advancement in the field. Considerable work was done during the first two years to optimize the growth of high-quality h-BN and transfer these onto H-terminated diamond substrates. These samples have been sent to DEVCOM ARL for device fabrication.

Creation of diamond-based heterointerfaces is the core of the project, and several such heterostructures have been synthesized and characterized. For the BN thin-

film growth, we installed the advanced-level load-lock IBPLD growth chamber. Since the PLD thin-film growth process involves several growth parameters, in the first phase, we tried to optimize as well as understand the growth evolution of BN thin films on various substrates and under various growth conditions (by varying all possible growth parameters). Films were characterized by several techniques (e.g., XRD, AFM, XPS, FTIR, Raman, and HRTEM). As observed, BN films grown on sapphire under HPTP conditions are important and show a nice crystalline quality. Furthermore, we found that in-situ annealing improves the surface quality. We adopted the same growth conditions to grow BN films on GaN substrates, as well as on both commercially purchased and home-grown PCD and SCD substrates. In some cases, we also performed in-situ annealing of films to improve the surface quality. From our in-depth extensive characterizations, films on an SCD substrate show the formation of possible nanocrystalline c-BN, however, without any long-range atomic ordering.

Considering the complex phase diagram of BN and related growth kinetics, to obtain highly crystalline c-BN–SCD films in the near future, we need to play with the growth parameters more and optimize those to grow epitaxial c-BN thin films on SCD substrates by PLD. One important parameter would be to grow films at much higher temperatures, possibly at 1000 °C, as for c-BN to form, a high growth temperature is an important factor. Another consideration would be to change the substrate crystalline facets, as different facets form different formation energies. Furthermore, in-situ or ex-situ high-temperature annealing (≥1000 °C) might also be needed to obtain pure-phase c-BN.

In addition, our aim is to grow c-BN films on not only along (001)-oriented SCD substrates, but also along different facets of SCD, for example, (111) and (113), with different miscut angles and surface roughnesses in order to understand the interfacial relationship between c-BN and SCD, and the consequent device potentials of c-BN–diamond heterostructures, with the ultimate goal of making high-mobility FET devices. We will continue to apply a strong theoretical effort to support our experimental activities including growth, surface modification, and doping in diamond.

Development of specific metrology for diamond-based structures has been another highlight during the second-year effort. Various new techniques, such as THz spectroscopy, SHG techniques, scanning probe techniques, and so on, have been explored to enable fast and efficient characterization of diamond surfaces to augment conventional imaging and spectroscopy methods. Characterizations of the materials have been done in synergy with DEVCOM ARL researchers and facilities at DEVCOM ARL. Some of the device structures fabricated at DEVCOM ARL are being characterized in detail at Rice using FIB slicing and HRTEM. More

importantly, the FIB milling procedure to prepare the TEM specimens of as-grown diamond wafers, diamond–BN heterointerfaces, and diamond-based FET devices is now optimized, and state-of-the-art microscopy methods are being employed to characterize the aforementioned systems at subnanometer resolution with the most accuracy. The details revealed from these studies will enable further optimization of the device architectures being developed at DEVCOM ARL.

A strong collaboration team has been built during the first year between teams at Rice and DEVCOM ARL. Interactions included bimonthly discussions via Microsoft Teams, phone calls, specimen exchanges, joint publications (several in the pipeline), and use of facilities at both sites. The third year will see strong interaction as the diamond substrates being grown at Rice will be directly used by DEVCOM ARL in device fabrication. The collaboration will extend to other DOD labs (Air Force Research Laboratory, Naval Research Laboratory) in the future. The work done during the second year lays the foundation for a long-term collaboration between Rice and DEVCOM ARL toward developing diamond-based UWBG electronic device for areas such as high-power and RF electronics. The facility established at Rice for diamond growth will also enable other applications of diamond-based materials such as quantum sensing and computing. The diamond devices built as part of this effort will also enable new opportunities in the network platforms that is being developed as part of the same CA.

10. References

1. Neudeck PG, Okojie RS, Chen LY. High-temperature electronics - a role for wide bandgap semiconductors? Proc IEEE. 2002;90(6):1065–1076. https://doi.org/10.1109/JPROC.2002.1021571.

2. Takahashi K, Yoshikawa A, Sandhu A, Ishitani Y, Kawakami Y. Wide bandgap semiconductors: fundamental properties and modern photonic and electronic devices. Springer; 2007. https://doi.org/10.1007/978-3-540-47235-3.

3. Davis RF, Sitar Z, Williams BE, Kong HS, Kim HJ, Palmour JW, Edmond JA, Ryu J, Glass JT, Carter CH. Critical evaluation of the status of the areas for future research regarding the wide band gap semiconductors diamond, gallium nitride and silicon carbide. Mater Sci Eng B. 1988;1(1):77–104. https://doi.org/10.1016/0921-5107(88)90032-3.

4. Chow TP, Tyagi R. Wide bandgap compound semiconductors for superior high-voltage unipolar power devices. IEEE Trans Electron Devices. 1994;41(8):1481–1483. https://doi.org/10.1109/16.297751.

5. May PW. Materials science: the new diamond age? Science. 2008;319(5869):1490–1491. https://doi.org/10.1126/science.1154949.

6. Pau M, B W. Diamond thin films: a 21st-century material. Phil Trans R Soc. 2000;358:473–495.

7. Saslow W, Bergstresser TK, Cohen ML. Band Structure and Optical Properties of Diamond. Phys Rev Lett. 1966;16(9):354. https://doi.org/DOI 10.1103/PhysRevLett.16.354.

8. Wei L, Kuo PK, Thomas RL, Anthony TR, Banholzer WF. Thermal conductivity of isotopically modified single crystal diamond. Phys Rev Lett. 1993;70:3764.

9. Suzuki K, Sawabe A, Yasuda H, Inuzuka T. Growth of diamond thin films by DC plasma chemical vapor deposition. Appl Phys Lett. 1987;50(12):728–729. https://doi.org/10.1063/1.98080.

10. Mokuno Y, Chayahara A, Yamada H. Synthesis of large single crystal diamond plates by high rate homoepitaxial growth using microwave plasma CVD and lift-off process. Diam Relat Mater. 2008;17(4–5):415–418. https://doi.org/10.1016/j.diamond.2007.12.058.

11. Strobel P, Riedel M, Ristein J, Ley L. Surface transfer doping of diamond. Nature 2004;430:439–441. https://doi.org/10.1038/nature02751.

12. Ajayan PM, Vajtai R, Zhang X, Puthirath AB, Oliviera E, Li C, Kannan H, Gray T, Ivanov T, Birdwell AG, et al. Development of diamond based materials systems for high-power RF electronics: first-year report. DEVCOM Army Research Laboratory (US); 2022 Mar. Report No.: ARL-TR-9414.

13 Tsao JY, Chowdhury S, Hollis MA, Jena D, Johnson NM, Jones KA, Kaplar RJ, Rajan S, de Walle CG, Bellotti E, et al. Ultrawide-bandgap semiconductors: research opportunities and challenges. Adv Electron Mater. 2018;4(1). https://doi.org/10.1002/aelm.201600501.

14. Bader SJ, Lee H, Chaudhuri R, Huang S, Hickman A, Molnar A, Xing HG, Jena D, Then HW, Chowdhury N, et al. Prospects for wide bandgap and ultrawide bandgap CMOS devices. IEEE Trans Electron Devices. 2020;67(10):4010–4020. https://doi.org/10.1109/TED.2020.3010471.

15. Monteiro SN, Skury ALD, de Azevedo MG, Bobrovnitchii GS. Cubic boron nitride competing with diamond as a superhard engineering material – an overview. J Mater Res Technol. 2013;2(1):68–74. https://doi.org/10.1016/j.jmrt.2013.03.004.

16. Kulisch W, Freudenstein R, Klett A, Plass MF. A concept for the deposition of adherent cubic boron nitride films. Thin Solid Films. 2000;377–378:170–176. https://doi.org/https://doi.org/10.1016/S0040-6090(00)01318-3.

17. Aziz MJ. Film growth mechanisms in pulsed laser deposition. Appl Phys A. 2008;93(3):579. https://doi.org/10.1007/s00339-008-4696-7.

18. Kim S, Fröch JE, Gardner A, Li C, Aharonovich I, Solntsev AS. Second-harmonic generation in multilayer hexagonal boron nitride flakes. Opt Lett. 2019:44(23):5792–5795. https://doi.org/10.1364/OL.44.005792.

19. Giannuzzi LA, Stevie FA. A review of focused ion beam milling techniques for tem specimen preparation. Micron. 1999;30(3):197–204. https://doi.org/https://doi.org/10.1016/S0968-4328(99)00005-0.

20. Hetherington C. Aberration correction for TEM. Mater Today. 2004;7(12):50–55. https://doi.org/https://doi.org/10.1016/S1369-7021(04)00571-1.

21. Crawford KG, Weil JD, Shah PB, Ruzmetov DA, Neupane MR, Kingkeo K, Birdwell AG, Ivanov TG. Diamond field-effect transistors with V_2O_5-induced transfer doping: scaling to 50-nm gate length. IEEE Trans Electron Devices. 2020;67(6). https://doi.org/10.1109/TED.2020.2989736.

22. Jin Z, Tkach A, Casper F, Spetter V, Grimm H, Thomas A, Kampfrath T, Bonn M, Kläui M, Turchinovich D. Accessing the fundamentals of magnetotransport

in metals with terahertz probes. Nat Phys. 2015;11(9):761–766. https://doi.org/10.1038/nphys3384.

23. Hilton DJ, Arikawa T, Kono J. Cyclotron resonance. Charact Mater. 2012 May 18:1–15. https://doi.org/https://doi.org/10.1002/0471266965.com068.pub2.

24. McGahan WA, Johs B, Woollam JA. Techniques for ellipsometric measurement of the thickness and optical constants of thin absorbing films. Thin Solid Films. 1993;234(1):443–446. https://doi.org/https://doi.org/10.1016/0040-6090(93)90303-7.

25. Li C, Zhang X, Oliveira EF, Puthirath AB, Neupane MR, Weil JD, Birdwell AG, Ivanov TG, Kong S, Gray T, et al. Systematic comparison of various oxidation treatments on diamond surface. carbon. 2021;182:725–734. https://doi.org/https://doi.org/10.1016/j.carbon.2021.06.050.

26. Coe SE, Sussmann RS. Optical, thermal and mechanical properties of CVD diamond. Diam Relat Mater. 2000;9(9–10):1726–1729. https://doi.org/10.1016/S0925-9635(00)00298-3.

27. Takeuchi D, Kato H, Ri GS, Yamada T, Vinod PR, Hwang D, Nebel CE, Okushi H, Yamasaki S. Direct observation of negative electron affinity in hydrogen-terminated diamond surfaces. Appl Phys Lett. 2005;86(15):1–3. https://doi.org/10.1063/1.1900925.

28. Williams OA, Jackman RB. Surface conductivity on hydrogen terminated diamond. Semicond. Sci Technol. 2003;18(3). https://doi.org/10.1088/0268-1242/18/3/305.

29. Ristein J, Riedel M, Ley L. Electrochemical surface transfer doping. J Electrochem Soc. 2004;151(10):E315. https://doi.org/10.1149/1.1785797.

30. Saha NC, Takahashi K, Imamura M, Kasu M. Observation of nitrogen species at Al_2O_3/NO_2/H-diamond interfaces by synchrotron radiation x-ray photoemission spectroscopy. J Appl Phys. 2020;128(13):1–6. https://doi.org/10.1063/5.0024040.

31. Hirama K, Sato H, Harada Y, Yamamoto H, Kasu M. Diamond field-effect transistors with 1.3 A/mm drain current density by Al_2O_3 passivation layer. Jpn J Appl Phys. 2012;51(9). https://doi.org/10.1143/JJAP.51.090112.

32. Geis MW, Fedynyshyn TH, Plaut ME, Wade TC, Wuorio CH, Vitale SA, Varghese JO, Grotjohn TA, Nemanich RJ, Hollis MA. Chemical and semiconducting properties of NO_2-activated H-terminated diamond. Diam

Relat Mater. 2018;84(2):86–94. https://doi.org/10.1016/j.diamond.2018.03.002.

33. Chandran M, Shasha M, Michaelson S, Hoffman A. Nitrogen termination of single crystal (100) diamond surface by radio frequency N_2 plasma process: an in-situ x-ray photoemission spectroscopy and secondary electron emission studies. Appl Phys Lett. 2015;107(11):2–6. https://doi.org/10.1063/1.4930945.

34. Hoffmann R, Kriele A, Obloh H, Hees J, Wolfer M, Smirnov W, Yang N, Nebel CE. Electrochemical hydrogen termination of boron-doped diamond. Appl Phys Lett. 2010;97(5):1–4. https://doi.org/10.1063/1.3476346.

35. Mirabedini PS, Debnath B, Neupane MR, Greaney PA, Birdwell AG, Ruzmetov D, Crawford KG, Shah P, Weil J, Ivanov TG. Structural and electronic properties of 2D (graphene, hBN)/H-terminated diamond (100) heterostructures. Appl Phys Lett. 2020;117:121901. doi: https://doi.org/10.1063/5.0020620.

36. Mirabedini PS, Neupane MR, Greaney PA. Ab initio study of the effect of 2D layer rippling on the electronic properties of 2D/H-terminated diamond (100) heterostructures. J Mater Res. 2021;36:4712–4724. https://doi.org/10.1557/s43578-021-00330-2.

List of Symbols, Abbreviations, and Acronyms

2-D	2-dimensional
2DHG	2-D hole gas
3-D	3-dimensional
a-BN	amorphous BN
AC	alternating current
AFM	atomic force microcopy
Al_2O_3	alumina/sapphire
Ar	argon
ARL	Army Research Laboratory
B	boron
BCN	boron carbon nitride
BDD	B-doped diamond
BFOM	Baliga figure of merit
BN	boron nitride
C	carbon
CA	Cooperative Agreement
c-BN	cubic BN
CR	cyclotron resonance
Cu	copper
CVD	chemical vapor deposition
DC	direct current
DEVCOM	US Army Combat Capabilities Development Command
DFT	density functional theory
DOD	Department of Defense
EDS	energy dispersive spectroscopy
EELS	electron energy loss spectroscopy

E_{int}	interfacial energy
ESCD	electronic-grade single-crystal diamond
FET	field-effect transistor
FIB	focused ion beam
FIR	far-IR
FTIR	Fourier transform IR
FWHM	full width at half maximum
Ga	gallium
GaN	gallium nitride
H/H_2	hydrogen
H_2O	water
H_2O_2	hydrogen peroxide
H_2SO_4	sulfuric acid
H_2SO_4	sulfuric acid
h-BCN	hexagonal BCN
HBDD	hydrogenated BBD
h-BN	hexagonal BN
HBr	hydrogen bromide
HD	hydrogenated diamond
HF	hydrofluoric acid
HNO_3	nitric acid
HPHT	high-pressure, high-temperature
HRTEM	high-resolution TEM
IBAPLD	ion-beam-assisted pulsed laser deposition
IR	infrared
KrF	krypton fluoride
$LiNbO_3$	lithium niobate
MBE	molecular beam epitaxy

Mo	molybdenum
MOSFET	metal–oxide–semiconductor field-effect transistor
MPCVD	microwave-plasma CVD
N	nitrogen
NEA	negative electron affinity
NO_2	nitrogen dioxide
O	oxygen
O-HBDD	oxidized HBDD
P	phosphorus
PCD	polycrystalline diamond
PLD	pulsed laser deposition
PMMA	poly(methyl methacrylate)
ReaxFF	reactive force field
RF	radio frequency
RHEED	reflection high-energy electron diffraction
RMD	reactive molecular simulations
S	sulfur
SCD	single-crystal diamond
SEM	scanning electron microscope
SHG	second-harmonic generation
Si	silicon
SiC	silicon carbide
SIMS	secondary ion mass spectrometry
SiO_2	silicon dioxide
STEM	scanning transmission electron microscopy
t-BN	turbostratic BN
TDS	time domain spectroscopy

TEM	transmission electron microscopy
THz	terahertz
TMO	transition metal oxide
UV	ultraviolet
UWBG	ultra-wide bandgap
V_{acc}	acceleration voltage
V_2O_5	vanadium pentoxide
XPS	X-ray photoelectron spectroscopy
XRD	X-ray powder diffraction
ZnTe	zinc telluride

1 (PDF)	DEFENSE TECHNICAL INFORMATION CTR DTIC OCA
1 (PDF)	DEVCOM ARL FCDD RLD DCI TECH LIB
10 (PDF)	DEVCOM ARL FCDD RLS ER T IVANOV A G BIRDWELL D RUZMETOV M NEUPANE P SHAH S RUDIN J WEIL L DE LA CRUZ D WASHINGTON FCDD RLS ED S B KELLEY